

# Crystal chemistry of amphiboles studied by Raman spectroscopy

---

Master Thesis in Geoscience

Mineralogisch-Petrographisches Institut

Universität Hamburg

-----

**Lisa Leißner**

Matrikel-Nr. 6126395

Adviser: PD Dr. Boriana Mihailova

Prof. Dr. Jochen Schlüter

Submission: 27.10.2014

# Crystal chemistry of amphiboles studied by Raman spectroscopy

# Content

1. Introduction .....	1
2. Materials and Methods .....	2
2.1. Amphiboles .....	2
2.1.1. Occurrence .....	2
2.1.2. Structure and chemistry.....	2
2.1.3. Classification.....	3
2.1.4. Samples used in this study .....	4
2.2. Analytical methods.....	5
2.2.1. Electron microprobe analysis .....	5
2.2.2. Raman spectroscopy.....	5
2.2.3. Experimental conditions used in this study.....	7
2.3 Spectroscopy of amphiboles .....	8
3. Results and discussion.....	12
3.1. Electron microprobe analysis .....	12
3.2. Raman spectroscopy.....	17
3.2.1. Spectral range of skeleton vibrations (15 – 1215 cm <sup>-1</sup> ).....	18
3.2.2. OH-bond stretching mode (3400 - 3800 cm <sup>-1</sup> ).....	19
3.3. Sources of errors.....	30
3.4. Comparison to infrared spectroscopic studies.....	31
4. Conclusion.....	34
4.1. Application.....	34
4.2. Summary .....	35
4.3. Further Work.....	35
References .....	37
Appendix .....	40
Erklärung.....	44
Danksagung.....	45

# Figures

Figure 1: Structure of monoclinic amphibole (yellow: A-site cations; purple: B-site cations; dark blue: T-site cation; light blue: M3 site cations; dark green: M1 site cations; grey: M2 site cations; red: oxygen; white: hydrogen). The figure was prepared using the VESTA software package (Momma & Izumi, 2008) with the data of Welch & Knight (1999). .....	3
Figure 2: Scheme of the classification of amphiboles. Amphibole subgroups marked in orange were analyzed in this study. ....	3
Figure 3: Absorption and scattering processes produced by incident laser beam. (after Nasdala et al., 2004) .....	6
Figure 4: The chemical bonding can be thought as a spring between atoms with masses $m$ and $M$ . The reduced mass $\mu$ is equal to $mM/(m+M)$ . $K$ is the force constant of the bonding .....	6
Figure 5: Top view of the orientation of the amphibole-needles in the Raman scattering experiments; see text for more details about the scattering geometries. ....	8
Figure 6: Polarizability tensors of the Raman-active modes in $C2/m$ with unique $b$ -axis. (Kroumova et al., 2003).....	8
Figure 7: A typical Raman spectrum of amphibole with $T = Si^{4+}$ and $W = OH^-$ . ....	9
Figure 8: Simplified schema to estimate the $Fe^{3+}$ content, following the IMA report on amphiboles 2012 (Hawthorne et al., 2012) including the diagram of Schumacher (1997) in the center to describe the recalculate criteria. ....	12
Figure 9: Comparison of $Mg^*$ -calculated by using own Excel spreadsheet and the Spreadsheet of Locock (2014). ....	14
Figure 10: Raman spectra of glaucophane sample (a13) measured in four experimental configurations.....	17
Figure 11: Slight mismatch of the Raman peak position due to the use of visible or UV laser.....	17
Figure 12: <b>Top:</b> Raman spectra in the range of $15-1215\text{ cm}^{-1}$ . On the left hand site, the spectra of glaucophane, show strong orientation dependence of the peak intensity in the range of $900-1100\text{ cm}^{-1}$ , arising from the $Si-O_{\text{non-bridging}}$ stretching mode. On the right hand site, the spectra of actinolite do not exhibit such dependence. <b>Bottom:</b> Macroscopically labeled horizontal/vertical orientation can mean two different orientations from structural view due to uncertainties in the orientation of the $b$ axis. On the left-hand side the polarization of the incident and scattering light is in the $(a-c)$ plane and the atomic vector displacement for the $Si-O_{\text{non-bridging}}$ stretching mode are either approximately parallel (vertical orientation) or perpendicular (horizontal orientation) to polarization of the incident light $E_i$ and scattering light $E_s$ . On the right-hand side is the photon polarization in the $(b-c)$ -plane, and atomic displacement vectors for $Si-O_{\text{non-bridging}}$ stretching mode are $\perp E_i$ and $E_s$ , in both vertical and horizontal orientation; hence the intensity is weakly dependent on the orientation. ....	18
Figure 13: Raman scattering of grunerite (a9) originating from OH-stretching modes. ....	19
Figure 14: Raman scattering of tremolite and richterite generated by OH-stretching modes. The peak shift of ca. $55\text{ cm}^{-1}$ is due to the A-site occupancies.....	19

Figure 15: Mg*-ratio, calculated from the Raman spectroscopic data versus the ratio calculated from electron microprobe analysis (Mg <sub>Li</sub> *). The red data point is obtained after taking into account possible Mg/Fe distribution on the B site. ....	20
Figure 16: The OH stretching modes of tremolite (a4, a18) and actinolite (a19) sample show better <sup>C</sup> Fe <sup>2+</sup> determination than the calculation scheme of electron microprobe analysis.....	21
Figure 17: Raman scattering of cummingtonite (a23) caused by OH-stretching modes.....	21
Figure 18: Peak fitting of the asymmetric tremolite samples a18, a10 and a4.....	22
Figure 19: Raman scattering caused by OH-stretching modes for glaucophane (a13), magnesio-arfvedsonite(a42) and tremolite (a37). These samples show continuous change in wavenumber due to the change in the B-site and C(M2)-site composition. ....	23
Figure 20: Raman scattering of <sup>C</sup> Al <sup>3+</sup> containing samples glaucophane (a13) and clino-ferro-holmquistite (a28) generated by OH-stretching modes. The small peak shift is due to variations in the B-site composition. ....	24
Figure 21: The OH-stretching mode of anthophyllite (a7) shows splitting in 3 peaks. The intensity of the highest wavenumber component (marked by the arrow) exhibits strong orientation-dependence.....	25
Figure 22: Sample a28 (clino-ferro-holmquistite) shows one orientation dependent peak, which changes in asymmetric shape from horizontal to vertical orientation.....	25
Figure 23: A site occupation and <sup>T</sup> Al <sup>3+</sup> content versus the full width at half maximum (FWHM) of OH bond stretching mode. ....	25
Figure 24: Tried A site calculations do not show usable results. ....	26
Figure 25: <b>Top:</b> Schematic presentation of the effect of fluorine with filled A site (after Robert et al. (1999)). <b>Bottom:</b> OH-stretching spectra of richterite and fluoro-edenite. Both samples have similar chemical composition. The major difference is the fluorine content. ....	27
Figure 26: Calculation of fluorine content following the procedure proposed by Robert et al. (1999).....	27
Figure 27: Filled A site (effect marked by the blue arrow), Al <sup>3+</sup> on the T site and F on the W site (effect marked by the violet arrow) of samples a34 and a35 caused wrong peak assignment to M1M1M3 species. ....	28
Figure 28: Raman scattering resulting from OH-stretching modes of richterite (a30) and <sup>C</sup> Li containing potassic-ferri-leakeite (a36). The negative peak shift of -30 cm <sup>-1</sup> may be due to <sup>C</sup> Li.....	28
Figure 29: Sample a26 shows strong continuum background due to fluorescence. The analysis of the Raman peaks could only be done after the baseline correction.....	30
Figure 30: Comparison of ferro-holmquistite (a28) and actinolite (a19). The position of the MgMgMg-OH-□-peak of a28 is close to the position of the MgMgFe-OH-□-peak of a19. This complicates the determination of the peaks. ....	34

# Tables

Table 1: Localities of the studied samples .....	4
Table 2: The phonon modes of amphibole with space group C2/m. Infrared-active modes are marked in red and Raman-active modes are marked in green.H1 is assumed to occupy (4i) Wyckoff position bonded to the adjacent oxygen O3. ....	9
Table 3: Chemical composition of the studied samples, determined by electron microprobe analysis. Samples with assumed Li <sup>+</sup> content (by total weight sum) are marked in red. ....	15
Table 4: Calculation of B-site occupancy based on the splitting of Raman OH-stretching peaks. ....	22
Table 5: Change in Li <sup>+</sup> assumption (marked in red) for sample a36 changes also the occupancy of A site (marked in green). Without additional measurements of Li <sup>+</sup> these calculations have to be handled with care. ....	26
Table 6: Comparison of the position of infrared (left) and Raman (right) peaks originating from OH-stretching modes. Data in good agreement are marked in blue. ....	32

# Zusammenfassung

Amphibole ( $A_{0-1}B_2C_5T_8O_{22}W_2$ ) sind weit verbreitete gesteinsbildende Minerale, die in fast allen geologischen Umgebungen auftreten. Sie haben eine komplexe chemische Zusammensetzung bei der Ionen an verschiedenen kristallographischen Positionen im Kristallgitter sitzen können. Des Weiteren treten OH-Gruppen und zum Teil auch Li auf, wodurch eine genaue Bestimmung der Kristallchemie mit Hilfe der Mikrosondenanalyse erschwert wird. In dieser Arbeit wurden 34 Proben mit der Elektronenstrahl Mikrosonde und dem Raman Spektroskop (orientierungs- und polarisations-abhängig) untersucht. Die OH-Schwingungen zeigen eine klare Abhängigkeit vom Mg-Fe Gehalt auf der C-Position (M1M1M3 Triplet), sowie von der Besetzung (oder nicht Besetzung) der A-Position. Mg-reiche oder Fe-reiche Amphibole zeigen im OH-Bereich des Raman-Spektrums nur einen Peak (dieser liegt bei einer nicht besetzten A-Position bei Mg-reichen Proben im Bereich von  $3660 - 3673 \text{ cm}^{-1}$  und bei Fe-reichen Proben bei  $3610 - 3620 \text{ cm}^{-1}$ ), während Proben mit mittlerer Mg-Fe-Gehalten bis zu vier Peaks zeigen. Anhand dieser lässt sich ein  $Mg^*$ -Wert ( $Mg/(Mg+Fe)$ ) berechnen, der gute Übereinstimmungen zu den Mikrosonden Ergebnissen aufweist. Mit einer besetzten A-Position treten die Peaks in einem Bereich von  $3670 - 3730 \text{ cm}^{-1}$  auf, während bei einer leeren A-Position die Peaks in einem Wellenzahlbereich von  $3610 - 3673 \text{ cm}^{-1}$  auftreten. Aufgrund sehr breiter Peaks bei einer besetzten A-Position und variablen Gehalt an F, ist eine genaue Berechnung der Verfüllung der A-Position nicht möglich. Des Weiteren lässt sich eine Aussage über die B-Position treffen, aufgrund von Aufspaltung von Peaks. Probleme in der Bestimmung der C-, A- und B-Position treten bei Proben mit Al auf der T-Position auf, da dies zu sehr breiten Peaks führt.

## Abstract

Amphiboles ( $A_{0-1}B_2C_5T_8O_{22}W_2$ ) are common rock building minerals that occur in a wide geological and petrologic range. The complex chemical composition, with ions that can occur at different crystallographic sites and including OH-groups and sometimes Li, hinders the proper crystallochemical determination only with microprobe analysis. In this study 34 samples were analyzed with electron microprobe analysis and (orientation and polarization dependent) Raman spectroscopy. The OH-stretching modes of the Raman spectra show strong dependence on the Mg-Fe content at the C site (M1M1M3 triplet) of amphiboles as well as on the occupancy of the A site. Mg-rich or Fe-rich samples show only one peak (vacant A site with Mg-rich C site:  $3660 - 3673 \text{ cm}^{-1}$ , vacant A site with Fe-rich C site:  $3610 - 3620 \text{ cm}^{-1}$ ), while intermediate compositions show up to four OH-stretching mode peaks. Assuming that Mg and Fe are randomly distributed over all three crystallographically distinguished C sites (M1, M2, M3), one can calculate the ratio  $Mg^*$  ( $Mg/(Mg+Fe)$ ) from the fractional Raman intensities. The obtained ratio is in good agreement with the results of electron microprobe analysis. In the case of filled A site, the OH Raman peaks appear in the range  $3670 - 3730 \text{ cm}^{-1}$ , whereas in the case of vacant A site, the peaks appear at

wavenumbers between 3610 – 3675  $\text{cm}^{-1}$ . Due to the large broadening of Raman peaks associated with a filled A site and various amount of F, the accurate calculation of A site filling is not possible. Furthermore, a semi-quantitative estimation of Mg and Fe content on the B site is possible via slight splitting of the Raman peaks. Problems in determination of C, A and B site appear with Al content on T site, which produce large peak broadening.



# 1. Introduction

Amphiboles ( $A_{0-1}B_2C_5T_8O_{22}W_2$ ) are common rock forming minerals that can be found in all geological environments. They have been attracting a continuously growing interest among the mineralogical community for multiple reasons: amphiboles can be used as geothermobarometers, they are asbestos minerals and even gemstones (Vinx, 2008). Amphiboles have complex crystal chemistry due to non-tetrahedral crystal positions, which can be occupied by different ions. For geothermometric or geobarometric applications it is important to know which crystallographic site is occupied by which ion (Holland & Blundy, 1994). Methods like electron microprobe analysis cannot distinguish different site occupancies. On the other hand, for diffraction analysis a separate single crystal or a powdered sample is necessary and therefore this method cannot be applied to identify mineral specimens in thin sections or whole rock samples. Raman spectroscopy is an analytical method easy to be handled and can be used to study crystal chemistry and structure. It is a non-destructive, preparation-free method, which in general can be applied to study samples of any shape, including mineral specimens in thin sections or embedded in rock samples (or a jewel which cannot be damaged). In contrast to electron microprobe analysis, light elements such as hydrogen and lithium can be detected by Raman spectroscopy via the corresponding atomic vibrations. Hence, a crystallochemical determination is possible via suitable Raman spectral “fingerprints”. There have been a lot of studies dedicated to the chemical determination of amphiboles via the OH-stretching modes measured by infrared spectroscopy (Della Ventura et al. (2005), Robert et al. (1999), Ishida & Hawthorne (2003), Iezzi et al. (2005), Iezzi et al. (2007), Hawthorne et al. (1997)). Similar to Raman spectroscopy, infrared (IR) spectroscopy is based on atomic vibrations, but in contrast to Raman spectroscopy it needs time-consuming preparation and the application of IR microspectroscopy to submillimeter-sized samples imbedded in a thin section or a rock sample is not straightforward. Concerning Raman spectroscopy analysis, there are studies on the skeleton-range modes like Apopei & Buzgar (2010), who have discriminated of different amphibole species on the basis of the vibrational modes in the range of 200 to 1200  $\text{cm}^{-1}$ . There are only few studies considering OH-stretching modes (Wang et al. (1988), Chen et al. (2004), Klopogge et al. (2001), Su et al. (2009)). Wang et al (1988) did Raman spectroscopy of the OH-range at cummingtonites. Chen et al. (2004) studied Chinese jade by Raman spectroscopy of OH-stretching modes, compared with PIXE analysis. A good fit between both techniques was reached. Klopogge et al. (2001) studied the Raman spectra of Li-containing holmquistite. All three studies showed that a determination of Fe-Mg content of the amphiboles due to the OH-stretching modes is possible, like that already done by infrared spectroscopy. Su et al. (2009) studied zoned amphiboles by infrared and Raman spectroscopy and reported a good agreement between both methods. However a detailed Raman-scattering study of the OH-stretching range with a number of samples of different amphibole subgroups and complex chemistry, like that performed by Apopei & Buzgar (2010) for the range 200-1200  $\text{cm}^{-1}$ , is still missing. The OH-range of amphibole samples with filled A site have not been studied so far. Therefore the objective of this study is to analyze the Raman scattering arising from OH groups in large variety of natural amphiboles covering the main subgroups to explore the potential of Raman spectroscopy to be used for non-destructive crystal-chemical analysis of amphiboles. Amphiboles with Al on the tetrahedral position are excluded from this study.

## 2. Materials and Methods

### 2.1. Amphiboles

#### 2.1.1. Occurrence

The amphibole group is a complex rock forming mineral group. Amphiboles are common minerals in all geological environments, especially in metamorphic (e.g. amphibolites, shists) and igneous rocks (e.g. granites) (Vinx, 2008). Amphiboles appear in ultramafic (SiO<sub>2</sub>-poor) to felsic and alkaline rocks (SiO<sub>2</sub>-rich) but they are most common in the intermediate range of SiO<sub>2</sub> content of rocks. The occurrence in plutonic rocks is more important than in volcanic rocks, though there they also occur (Deer et al., 1980). Several amphiboles occur in asbestos form (eg. tremolite, actinolite, anthophyllite, grunerite and riebeckite) (Gunter et al., 2007) or as gemstones (eg. nephrite jade).

#### 2.1.2. Structure and chemistry

Amphiboles belong to inosilicates (chain silicates), which are built of double chains of corner-sharing TO<sub>4</sub> tetrahedra with T predominantly occupied by Si (Deer et al., 1980). They form fibrous, needle-like crystals elongated along the crystallographic c axis. Amphiboles occur in monoclinic and orthorhombic symmetry but the monoclinic structure is more common. Monoclinic amphiboles (clinoamphiboles) have space group *C2/m* (Hawthorne & Oberti, 2007). Orthorhombic amphiboles (orthoamphiboles) can have space group *Pnma* or *Pnmm* (Hawthorne & Oberti, 2007). The general chemical formula of amphibole can be written as: A<sub>0-1</sub>B<sub>2</sub>C<sub>5</sub>T<sub>8</sub>O<sub>22</sub>W<sub>2</sub>. The different letters symbolize different crystallographic positions (figure 1). The W site is most commonly occupied by OH<sup>-</sup> groups, but can also contain F<sup>-</sup>, Cl<sup>-</sup>, and O<sup>2-</sup>. The T site is tetrahedrally coordinated and separated into two types of crystallographically non-equivalent sites: 4xT1 and 4xT2. The T-site cations are mostly Si<sup>4+</sup>, less Al<sup>3+</sup> and Ti<sup>4+</sup>, where Al<sup>3+</sup> prefers the T1 site. The C-site cations are octahedrally coordinated. They are spread over three types of crystallographically non-equivalent sites: two M1-, two M2-, and one M3-site. The M1-sites and M3-site cations are bonded to the OH<sup>-</sup> groups, whereas the M2-site cations are bonded only to O<sup>2-</sup> anions. All three types of C sites (M1, M2, M3) can be occupied by Mg<sup>2+</sup>, Fe<sup>2+</sup>, Fe<sup>3+</sup>, Al<sup>3+</sup>, Mn<sup>2+</sup> and a lot of other ions. The M2 site is the smallest octahedral site and is preferred by high-charge cations like Fe<sup>3+</sup> (Oberti et al., 2007). The B site is also referred as M4 site. It can be occupied by Ca<sup>2+</sup>, Na<sup>+</sup>, Mg<sup>2+</sup>, Mn<sup>2+</sup> or Fe<sup>2+</sup>. B-site cations are six-fold to eight-fold coordinated, as eight-fold coordination is common for large ions, such as Ca<sup>2+</sup>, whereas six-fold coordination is typical of smaller ions like Mg<sup>2+</sup> or Fe<sup>2+</sup>. The A-site cations are ten-fold to 12-fold coordinated. It is the largest site, which is occupied by Ca<sup>2+</sup>, Na<sup>+</sup> or K<sup>+</sup>, or is vacant to ensure electron neutrality of the amphibole unit cell (Deer et al. (1980), Okrusch & Matthes (2014), Hawthorne (1981), Markl (2008)).

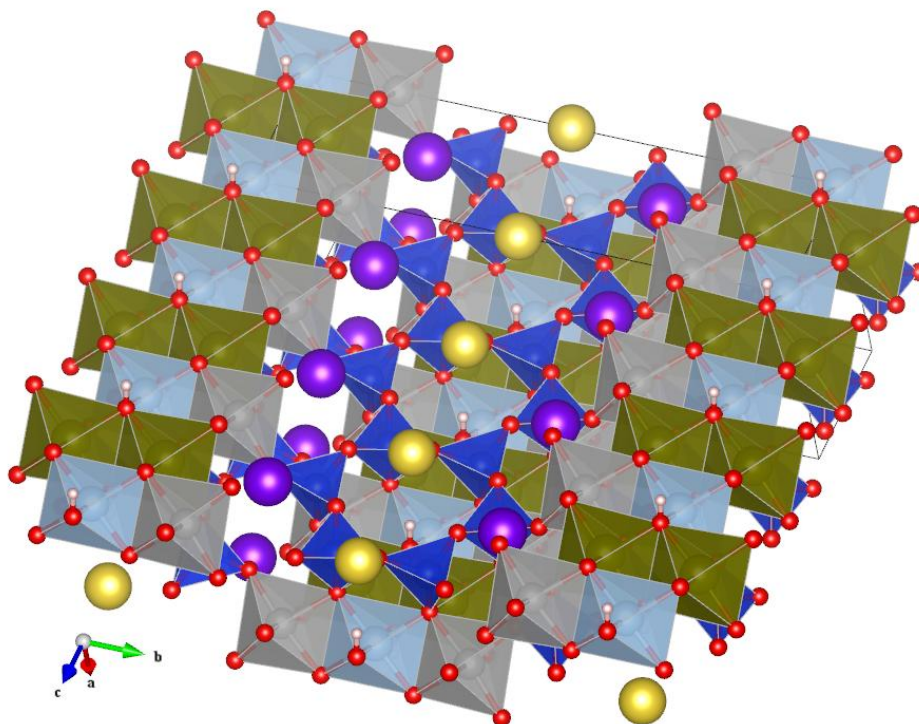


Figure 1: Structure of monoclinic amphibole (yellow: A-site cations; purple: B-site cations; dark blue: T-site cation; light blue: M3 site cations; dark green: M1 site cations; grey: M2 site cations; red: oxygen; white: hydrogen). The figure was prepared using the VESTA software package (Momma & Izumi, 2008) with the data of Welch & Knight (1999).

### 2.1.3. Classification

The nomenclature of the amphibole group was defined by the Amphibole Subcommittee of the Commission on New Minerals, Nomenclature and Classification (CNMNC) of the International Mineralogical Association (IMA). The newest classification of the amphibole group is published as an IMA report in 2012 (Hawthorne et al., 2012). In this thesis only a short summary of the classification

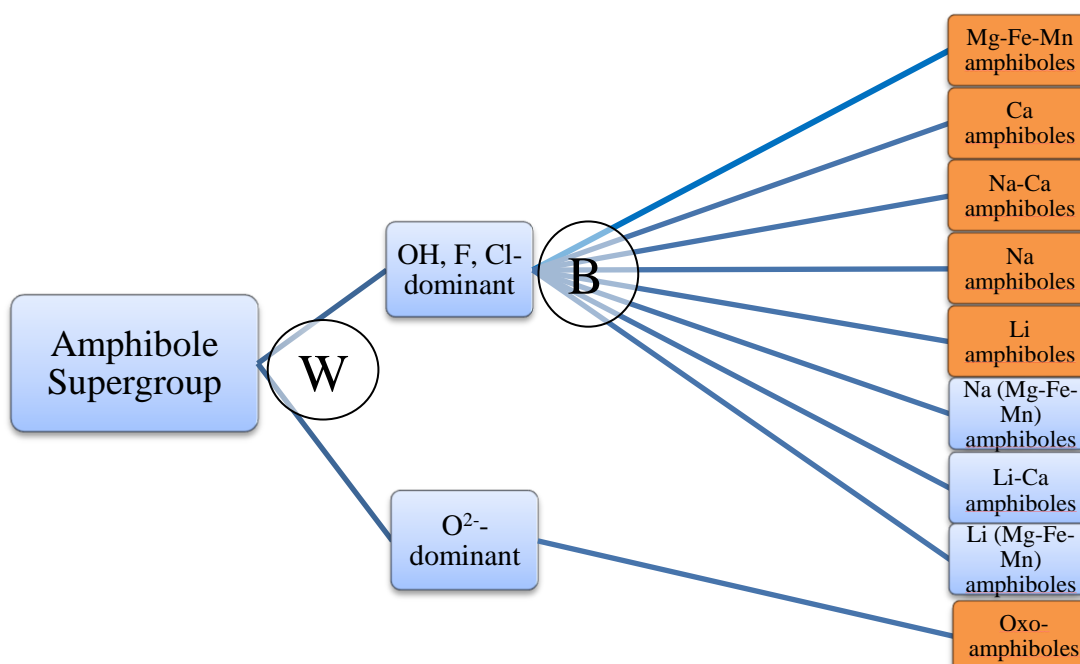


Figure 2: Scheme of the classification of amphiboles. Amphibole subgroups marked in orange were analyzed in this study.

is given. Details can be found in Hawthorne et al. (2012). The classification is based on the A, B and C site cations and the W site anions. The amphibole supergroup is first subdivided into two groups by the type of the dominant W-anion: O<sup>2-</sup>-dominant (oxo-amphiboles) and (OH<sup>-</sup>, F<sup>-</sup>, Cl<sup>-</sup>)-dominant. Depending on the composition of the B site, the group with dominant (OH<sup>-</sup>, F<sup>-</sup>, Cl<sup>-</sup>)-anions on the W site is further subdivided into eight subgroups: Mg-Fe-Mn-amphiboles, Na-Ca-amphiboles, Ca-amphiboles, Na-amphiboles, Li-amphiboles, Na-(Mg-Fe-Mn)-amphiboles, Li-Ca-amphiboles and Li-(Mg-Fe-Mn)-amphiboles (figure 2). Following these subdivisions the naming of amphibole depends on the composition of its dominant trivalent cations (and Ti<sup>4+</sup>) on the C site and additionally the composition of the A site.

#### 2.1.4. Samples used in this study

Only amphiboles with T site occupied by Si<sup>4+</sup> cations were chosen to be used in this study. Hence, the influence of Al<sup>3+</sup> on the T site was not part of this work. Nevertheless some samples turn out to contain also Al<sup>3+</sup> at T site. Nearly all samples are part of the mineral reference collection of the Mineralogical Museum of the University of Hamburg. Sample a39 was kindly provided by the Museum für Naturkunde Berlin and samples a41 and a42 were kindly provided by the TU Bergakademie Freiberg. The localities of the samples are listed in Table 1.

Table 1: Localities of the studied samples

Sample	Locality	Sample	Locality
a4	Sulzbachtal, Tyrol, Austria	a25	Snarum, Norway
a5	Campolungo, Tessin, Switzerland	a26	Garpenberg, Sweden
a6	Finland	a27	Uto, Sweden
a7	Snarum, Norway	a28	Goltsy, Siberia, Russia
a9	Westland, South Island, New Zealand	a29	Wilberforce, Ontario, Canada
a10	Nuristan, Afghanistan	a30	Kiran, Koksha Valley, Afghanistan
a10p	Samalpatti, Tamil Nadu, India	a31	Norra Kärr, Sweden
a12	Lofoten, Narvik, Norway	a33	Norra Kärr, Sweden
a13	Pollone, Piedmont, Italy	a34	Tuperssuatsiat, Greenland
a15	Sijlinjärvi b. Kuopio, Finland	a35	Kangerdluarsuq, Greenland
a16	Lydenburg, Transvaal, South Afrika	a36	Lovozero, Murmanskoya, Oblast, Kola, Russia
a17	Haugen, Oslo, Norway	a37	Tirodi Mine, Tirodi, Madhya Pradesh, India
a18	St. Gotthard, Switzerland	a38	Goldcamp Road, Colorado, USA
a19	Zillertal, Tyrol, Austria	a39	Sitapur, Chhindwara, Madhya Pradesh, India
a21	Stemmar-Thiersheim, Fichtelgebirge, Germany	a40	Umanaks fjord, Northgreenland
a23	Ochre, Alps I Mondei, Monteschebo (Navara), Italy	a41	Bong Mine, Bong Town, Bong Co., Liberia
a24	New Kryton Mohave Co., Arizona, USA	a42	Area-Netra-Ramrama Mine, Balaghat Dist., Madhya Pradesh, India

## 2.2. Analytical methods

### 2.2.1. Electron microprobe analysis

The electron microprobe analysis is a common method to analyze the chemistry of solid samples. The basic principles of the method are as follows. High-energy electrons are shot onto the sample. The energy of the electron beam matches the bound energy of the inner-shell electrons. Therefore upon electron beam irradiation, the core electrons can be excited from their ground level to the unoccupied valence level or to the conduction zone. As a result there is a vacancy at inner-shell electron levels. This vacancy is energetically preferred for all outer-shell electrons and hence it is filled by another electron from a higher electron level. During this electron transition X-ray radiation is emitted. The energy of this X-ray radiation is specific for each chemical element and can be analyzed by the so-called energy-dispersive or wavelength-dispersive method. While the energy-dispersive method scans all wavelengths at the same time, the wavelength-dispersive method scans only the wavelength where the specific X-ray radiation is expected for the probed element. Therefore the energy-dispersive method, which is used for chemical analysis with the SEM (scanning electron microscope), is much faster but has a lower resolution. The wavelength-dispersive method, used in electron microprobe analysis (EMP) is time consuming but accurate. By comparison the intensities of the X-ray emission peaks with those from standard samples a qualitative analysis is possible. The detection of elements with  $Z$  lower than 5 (H, He, Li, Be) is not possible due to restrictions in the sensitivity of available detectors. In addition, it is not possible to distinguish between heterovalent cations of the same element. Therefore a determination of ferric ( $\text{Fe}^{3+}$ ) and ferrous iron ( $\text{Fe}^{2+}$ ) is not executable (Klein & Philpotts, 2013).

### 2.2.2. Raman spectroscopy

Light is a mixture of electromagnetic waves, with oscillating mutually perpendicular electric and magnetic field, which are also perpendicular to the propagating direction of energy. From quantum mechanical point of view light is composed of photon. Raman spectroscopy is based on the Raman effect: the inelastic light scattering by atomic vibrations. In quantum mechanics collectivized vibrational energy is not random but composed of vibrational quanta. These lattice vibrations in crystals are called phonons and can be separated in optical and acoustic. While the acoustic phonons oscillate in-phase, the optical oscillate out-of-phase. Optical phonons possess induced dipole moment. The induced dipole moment can be due to the change in atomic positions (infrared-active) or due to the deformation of electron-shell (Raman-active). While a sample is irradiated by a monochromatic laser beam (near-IR, visible, or UV) with frequency  $\nu_0$ , different scattering processes can occur. The most intense effect is the Rayleigh scattering. This is an elastic process where the system is excited to a virtual high energy level and recovers immediately without a change in the photon energy, i.e. the same frequency like incidence ( $\nu_0$ ) is scattered back ( $\nu_0$ ). The other, much weaker, process is the Raman scattering, where intensity is approximately  $10^{-4}$  less than the intensity of Rayleigh scattering. This is an inelastic process where photon energy is lost or gained during the scattering, due to excitations of phonons in crystals, collective vibrations in glasses or molecule vibrations in liquids and gases. The scattered frequency  $\nu_s$  differs from the incident frequency  $\nu_0$  by the

vibrational (phonon) frequency  $\nu_m$ ,  $\nu_s = \nu_0 \pm \nu_m$  ( $\nu_m \ll \nu_0$ ). The difference between the scattering and incident light is called Raman shift and thus the positions of the Raman peaks correspond to normal vibrational (phonon) states of the material under study. In the Stokes process the scattered light loses energy  $\nu_0 - \nu_m$ , due to the recover to a higher energetic state of the phonon than before. The absorption of photon energy by the crystal is due to the excitation from the ground vibrational state to the higher-energy vibrational state. In the anti-Stokes process there is an energy gain of scattered light  $\nu_0 + \nu_m$ . At room temperature the Stokes process is much stronger, because more phonons are on the ground state than on the excited state. Because Stokes and anti-Stokes Raman shifts have the same frequency while the Stokes Raman peaks are

much more intense, normally only Stokes Raman scattering is measured. In figure 3 the processes are illustrated as quantum-mechanical model. The virtual state is not a real stable state, but it is metastable and can be considered as existing for instantaneously small time during the complex

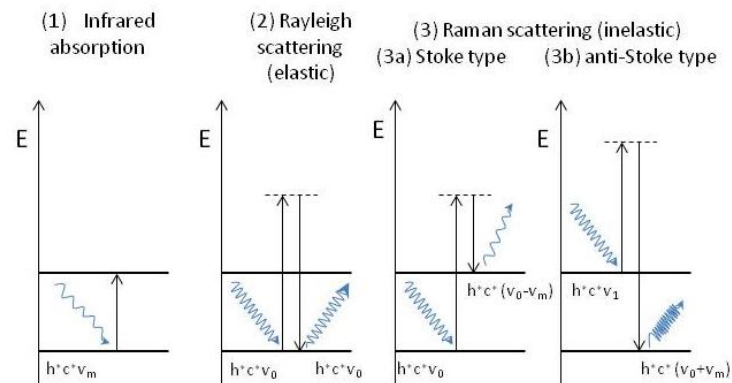


Figure 3: Absorption and scattering processes produced by incident laser beam. (after Nasdala et al., 2004)

interaction between photon an electrons and phonons in crystals. The reason for Raman scattering is the time-dependent polarizability of the chemical bonds. The time-dependence of polarizability is due to the ability of electrons to be displaced with respect to the corresponding nuclei, which are too heavy to follow the high-frequency oscillation of the electric field of light. Therefore the polarizability is strongly influenced by the vibrations of the atoms of the crystal. Hence Raman-active modes are those for which the rate of change of polarizability with vibrations is not zero. This is also the main difference to infrared-active modes, where the energy of the incident light corresponds to a vibrational energy and the interaction depends on the dipole moment induced by change in the centres of gravity of positively charged and negatively charged ions. In both infrared and Raman spectroscopy the peak positions are given in wavenumbers  $\omega$ ,  $\omega = \nu/c$ , where  $\nu$  is the vibrational frequency and  $c$  is the velocity of light. The phonon wavenumber depends strongly on the masses of the vibration atoms and on the chemical bonding:  $\omega = \sqrt{K/\mu}$ , where  $K$  is a force constant, which describes the bonding, and  $\mu$  is the reduced mass of the involved atoms, see figure 4. Each Raman band therefore is controlled by the involved atoms (mass, valence, size) and their bonds (strength and orientation). Therefore the spectra are specific for both chemistry and structure of crystals. The intensity of Raman scattering is proportional to the number of influenced atoms. The dynamic behaviour of the whole crystal can be distinguished by a unique cell, due to the larger wavelength of incident radiation than the unit-cell dimension (Ferraro et al. (2003), Rull (2012), Nasdala et al. (2004)).

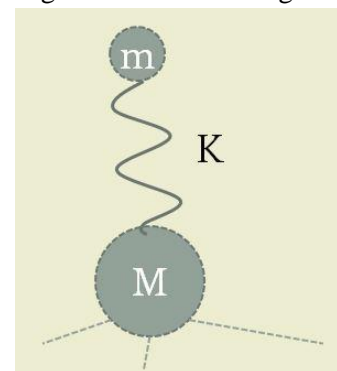


Figure 4: The chemical bonding can be thought as a spring between atoms with masses  $m$  and  $M$ . The reduced mass  $\mu$  is equal to  $mM/(m+M)$ .  $K$  is the force constant of the bonding.

Raman spectroscopy is orientation dependent. Most minerals, including amphiboles, are anisotropic. They have direction depending properties. The polarizability tensor mentioned above is a second-rank tensor, and therefore represents the anisotropy of the samples, that can be seen in Raman spectroscopy. The electric field vector of incident light is polarized in the plane perpendicular to the propagation of light. Therefore the declaration of analyzed orientations and polarizations is important. This can be done by Porto's notation: A(BC)D, where A and D stands for the propagation of incident and scattered light and B and C stands for the direction of the polarization of incident and scattered light. B and C therefore represent the components of the polarizability tensor and are characteristic for the point group. With different orientations of the sample as well as cross- and parallel polarized light the components of the polarizability tensor can be analyzed. Therefore a polarized Raman scattering analysis can characterize the vibrational symmetry of the sample. In the parallel polarized experiments (here notation HH (= horizontal horizontal) is used) the polarization of incident light is the same polarization that is measured of the scattered light. In contrast with cross polarized light (here the notation VH (= vertical horizontal) is used), the measured scattered polarization of the light is 90° rotated. Thereby the depolarization ratio ( $\rho = I_{\text{cross}}/I_{\text{parallel}}$ ) can be estimated. (Ferraro et al. (2003), Rull (2012), Nasdala et al. (2004))

### 2.2.3. Experimental conditions used in this study

34 amphibole specimens labelled a#, where # is the corresponding number, have been analyzed during this study. All samples were characterized by Raman spectroscopy and electron microprobe analysis.

The electron microprobe analysis was performed with a Cameca SX-100 SEM system with wavelength-dispersive detector at the Institute of Mineralogy and Petrology, University of Hamburg. The energy of the electron beam was 15 keV and the beam current was 20 nA. The following standards were used: F on LiF, Na on albite, Mg on MgO, Al on Al<sub>2</sub>O<sub>3</sub>, Si, Ca, Fe on andradite, Cl on vanadinite, K on orthoclase, Ti, Mn on MnTiO<sub>3</sub>, Cr on Cr<sub>3</sub>O<sub>3</sub>, Zn on Pb-glass, Sr on SrTiO<sub>3</sub> and Ba on Ba-glass. The beam acquisition time were 60 s for F, Na, Cl, K, Ti, Cr, Mn, Zn, Sr and Ba, 30 s for Ca, 20 s for Mg, Al and Fe and 10 s for Si. For samples a4-a24 with the exception of a10, a12, a15, a16, a17 50 points were measured. For all other samples 25 points were measured. The points were measured along one line across the sample or for small samples two (a5, a6, a9, a16, a24, a25, a26, a31, a36 and a38) or three (a7) lines were measured, to get enough measure points.

Raman experiments were conducted with a the Horiba Jobin-Yvon T640000 triple-grating spectrometer equipped with an Olympus BX41 microscope at the Institute of Mineralogy and Petrology, University of Hamburg. With the exception of samples a5, a6 and a7, all samples were measured with the green line of an Ar<sup>+</sup> laser ( $\lambda = 514.532$  nm) in the spectral range 15-1215 cm<sup>-1</sup> and 2600-3800 cm<sup>-1</sup>. The output laser power was 0.6 W for samples a5, a4, a9, a10, a10p, a12, a13, a15, a16, a17, a18, a19, a21, a23, a24, a26 and 0.44 W for samples a25, a27 to a41. The laser power was additionally reduced by a neutral density filter of 0.6 ( $10^{-0.6} = 0.25$  transmission intensity) on the laser beam pathway, with the exception of samples a12 and a24, for which filter 1 ( $10^{-1} = 0.1$  transmission intensity) was used. Samples a5, a6 and a7 showed a very strong photoluminescence when irradiated

with visible light and therefore they were measured with CdHe UV laser emitting at 325 nm with a laser power of 29 mW, without a filter. In this case the Raman scattering was collected in the whole range of 12-4000  $\text{cm}^{-1}$ . The acquisition time varied between 15 to 60 s depending on the sample. For most samples the signal-to-noise ratio was improved by averaging the spectrum over 10 loops. The spectra measured from samples a10, a13 and a21 were averaged over 15 loops, a10p over 20 loops, a17 over 7 loops and a24 over 5

loops. The achieved spectral resolution was  $\sim 2 \text{ cm}^{-1}$  with a visible laser and  $3 \text{ cm}^{-1}$  with a UV laser. The accuracy in determining the peak positions was  $0.35 \text{ cm}^{-1}$  and  $\sim 1 \text{ cm}^{-1}$  for 514.5 nm and 325 nm laser, respectively. All Raman spectra were measured in vertical and horizontal orientation of the sample (figure 5) both with parallel (HH) and cross-polarized (VH) light, in  $180^\circ$ -scattering geometry.

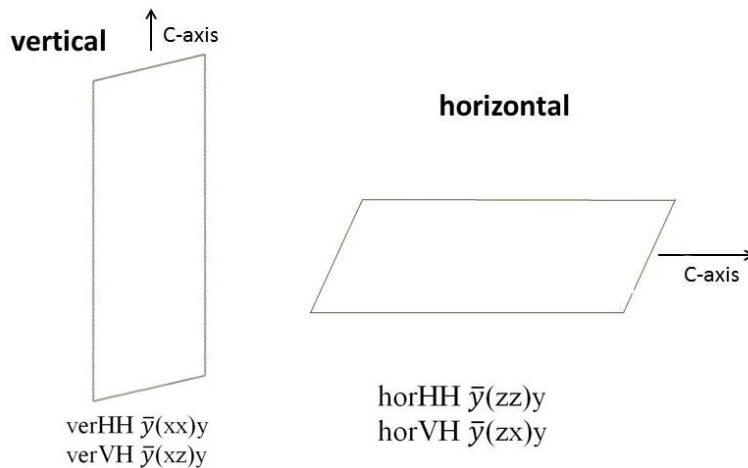


Figure 5: Top view of the orientation of the amphibole-needles in the Raman scattering experiments; see text for more details about the scattering geometries.

## 2.3 Spectroscopy of amphiboles

Initially, the investigation of amphiboles with spectroscopic methods was mainly applied to asbestos fibres to determine different species. Therefore, there are many studies about Raman spectroscopy of amphiboles, mainly in the lower spectral range. Most of them do not consider the spectral range of OH bond stretching.

In crystals there are  $3N-3$  optical phonons, where  $N$  is the number of atoms in the unit cell. For monoclinic amphiboles with the space group  $C2/m$ , which are more common, that means  $3 \cdot 42 - 3 = 123$  optical vibrational modes and 126 degrees of freedom (table 2). Of these three are acoustic modes:  $\Gamma_{\text{acoustic}} = A_u + 2B_u$  and 123 are optic modes  $\Gamma_{\text{optic}} = 30 A_g + 30 B_g + 28 A_u + 35 B_u$ .  $A_g$  and  $B_g$  are Raman-active whereas  $A_u$  and  $B_u$  are IR-active. Therefore 60 modes ( $30 A_g + 30 B_g$ ) are expected to generate Raman peaks, if the site symmetry of H1 is (4i). The hydrogen atoms can occupy (8j) Wyckoff Position with occupancy factor 0.5. The OH-stretching modes in this case will be discussed in detail later. The Raman polarizability tensors for the space group  $C2/m$  with unique b-axis are shown in figure 6.

**Raman Tensors**

$A_g$			$B_g$		
b	·	d	·	f	·
·	c	·	f	·	e
d	·	a	·	e	·

Figure 6: Polarizability tensors of the Raman-active modes in  $C2/m$  with unique b-axis. (Kroumova et al., 2003)



Table 2: The phonon modes of amphibole with space group  $C2/m$ . Infrared-active modes are marked in red and Raman-active modes are marked in green. H1 is assumed to occupy (4i) Wyckoff position bonded to the adjacent oxygen O3.

structure	wyckoff position	C2/m unique b-axis			
		$A_u$	$B_u$	$A_g$	$B_g$
T1	8j	3	3	3	3
T2	8j	3	3	3	3
M1	4h	1	2	1	2
M2	4g	1	2	1	2
M3	2a	1	2		
M4	4h	1	2	1	2
A	2b	1	2		
O1	8j	3	3	3	3
O2	8j	3	3	3	3
O3	4i	1	2	2	1
O4	8j	3	3	3	3
O5	8j	3	3	3	3
O6	8j	3	3	3	3
O7	4i	1	2	2	1
H1	4i	1	2	2	1

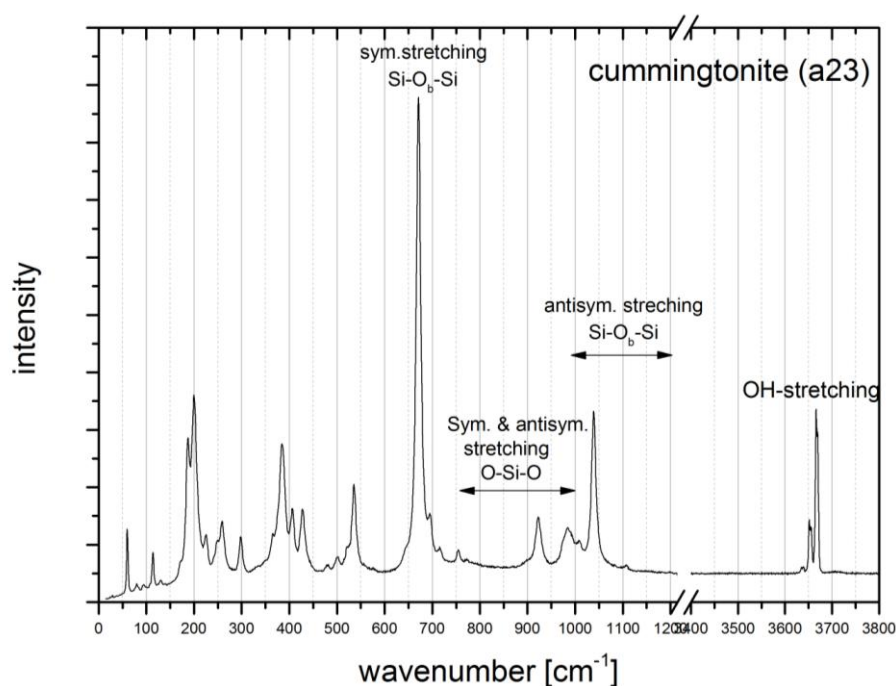


Figure 7: A typical Raman spectrum of amphibole with  $T = Si^{4+}$  and  $W = OH$ .

Figure 7 shows the spectrum of sample a23 in the range of  $15-1215\text{ cm}^{-1}$  and  $3400-3800\text{ cm}^{-1}$ . The origin of Raman scattering in the range below  $625\text{ cm}^{-1}$  is complex. Different authors attribute the observed peaks to different modes. Apopei & Buzgar (2010) present a short summary of the different opinions. Some of the named explanations are: vibrational modes of the non-tetrahedral cations, bending modes of

$SiO_4$  tetrahedra, OH libration and translation modes, lattice vibrations modes and translational M-OH modes (Apopei & Buzgar, 2010). The proper determination of the origin of the observed peaks is also hindered by the peak overlapping in this range. Hence, non-ambiguous peak assignment is still not available in literature. The range from  $625$  to  $1215\text{ cm}^{-1}$  is easier to be understood and investigated. The Raman scattering in this spectral range is dominated by  $SiO_4$  stretching modes as well as by vibrations of bridging oxygen atoms that link the adjacent  $SiO_4$  tetrahedra. The latter most probably

generate the strongest peak in most amphibole spectra, which is observed in the range of 650-750  $\text{cm}^{-1}$ . This type of atomic vibrations is called the breathing mode of the  $\text{SiO}_4$  ring, in which all bridging oxygen atoms vibrate in phase in the plane of the corresponding Si-O-Si bond angles. Other, sometimes strong, bands are found in the range of 750-950  $\text{cm}^{-1}$  (symmetric  $\text{SiO}_4$  stretching), 950-1000  $\text{cm}^{-1}$  (antisymmetric  $\text{SiO}_4$  stretching) and 1000-1215  $\text{cm}^{-1}$  (antisymmetric Si-O<sub>b</sub>-Si bond stretching) (Apopei & Buzgar, 2010). The OH bond stretching modes appear in the range 3600-3800  $\text{cm}^{-1}$ . M3M1M1 form a nearly equilateral triangle around each OH group. According to group theory hydrogen atoms on the 4i or 8j site generate crystal phonon modes which are either IR active ( $A_u$  and  $B_u$ ) or Raman active ( $A_g$  and  $B_g$ ). However, due to the same type of generating atomic vibration, i.e. same force constant and reduced mass, the wavenumbers of IR-active OH-stretching and Raman active OH-stretching in amphiboles are almost the same. Hence, the positions of IR and Raman peaks arising from OH-bond stretching should be very close to each other. Indeed, the experimental study by Apopei & Buzgar (2010) has revealed frequency difference of 2-3  $\text{cm}^{-1}$  between the position of the corresponding Raman and infrared peaks.

Because there are few studies about the OH range in Raman spectra, here the results from the infrared spectroscopy are briefly presented. The range of OH-stretching modes is well studied by infrared spectroscopy. The O-H group has one bond with a force constant  $K$  and one reduced mass. Considering the OH group as a diatomic molecule there should be  $(3 \times 2) - 5 = 1$  vibrational normal mode (Nasdala et al., 2004). Therefore only one peak should appear in the Raman spectra if we consider the OH groups as isolated units. However the  $\text{O}^{2-}$  of the OH is also shared between two  $\text{M1O}_6$  and one  $\text{M3O}_6$  octahedra, i.e. it is bonded to three octahedrally-coordinated cations and hence, the OH groups in amphiboles are not isolated units at all. Therefore, the proper analysis requires the application of site symmetry group theory to hydrogen atoms (Table 2, last row). By considering the directions of atomic vector displacements with respect to the O-H bonds, one can see that there is only one totally symmetric irreducible representation  $A_g$  related to H atoms on 4i or 8j Wyckoff positions, in which H atoms vibrate approximately along the O-H bonds, i.e. which is OH bond stretching (Bilbao server, Kroumova et al., 2003). The parallel polarized Raman spectra, which exhibit the strongest peaks, are dominated by  $A_g$  modes. Therefore, from pure crystallographic point of view a single Raman peak in the range of OH bond stretching should be expected. The strength of O-H bonding strongly depends on the chemical environment; especially of the C site (M1M1M3 triplet) and the A site (Hawthorne & Della Ventura, 2007). The variation in the chemical surroundings of the individual OH groups result in more than one peak in the range of OH bond stretching. These variations on the OH-stretching modes could be derived from the changes in C-(M1M1M3-) and A-site. Considering the substitution of  $\text{Fe}^{2+}$  for  $\text{Mg}^{2+}$  on the M1 or M3 site, the higher electronegativity of  $\text{Fe}^{2+}$  increases the strength of  $\text{Fe}^{2+}$ - $\text{O}^{2-}$  bonding, which in turn weakens the O-H bonding and the force constant  $K_{(\text{O-H})}$  decreases. The frequencies of the peak should therefore decrease towards lower wavenumbers if the number of  $\text{Fe}^{2+}$  adjacent to  $\text{O}^{2-}$  increases. The O-H bonding is of covalent character and therefore the so called two-mode behaviour is expected for the OH bond stretching. This means that OH groups bound to chemically different M1M1M3 triplets generate Raman peaks at different positions, with fractional integrated intensities proportional to the concentration of different chemical species. If we consider only Mg and Fe on the C site, the possible chemical M1M1M3

species are MgMgMg, MgMgFe, MgFeFe, and FeFeFe. Therefore, up to four OH-stretching peaks can be observed due to chemical variations on the M1 and M3 sites.

The filled A site has positive charge and leads to repulsive interactions with the  $H^+$  cation. This leads to a confined space for the motion of  $H^+$  and restricts the freedom of the OH bond vibrational stretching. Effectively, this results in stronger O-H bonding, i.e. higher force constant  $K_{(O-H)}$  and therefore higher frequencies of the corresponding Raman peak. Thus more than one peak can appear also depending on the occupancy of the A site. Because of short-range and nearest-neighbour environment disorder overlapping of bands can occur and produce broad peaks. Hawthorne & Della Ventura (2007) have supposed that when A-site is partially filled, additional coupling of energetically and physically close bands may lead to peak-broadening. A-site filled peaks have full width half maxima (FWHM) of  $25\text{ cm}^{-1}$  while A-site vacant peaks have FWHM of  $2\text{ cm}^{-1}$ . Peak broadening may also occur due to the energy distribution of the OH bond stretching induced by chemical disorder. Although the OH bond stretching is mainly affected by the M1M1M3 triplet and A site; T-, M2-, and M4-site, as well as fluorine on the W site can also influence the OH-peaks. (Hawthorne & Della Ventura, 2007) Substitution on T site (e.g.  $Si^{4+}$  and  $Al^{3+}$ ), like in pargasite and kaersutite, leads to broad infrared peaks in the OH-range. The H atoms in monoclinic amphiboles can have hydrogen-bonding to the O7 atoms, which are bonded to T1-site cations. Through this hydrogen bonding the chemistry of the T site can influence the OH-stretching mode. By infrared spectroscopy a shift of about  $-20\text{ cm}^{-1}$  was measured also due to substitution of  $Al^{3+}$  for  $Si^{4+}$  on T site (Hawthorne & Oberti, 2007). In some OH spectra a subtle peak splitting appear. Different authors relate this to the sole M4-site effect (Chen et al. (2004), Gottschalk & Andrut (1998)) or combined M4- and M2-site effect (Hawthorne & Della Ventura (2007), Iezzi et al. (2005)). How exactly this sites interact with the OH-bond is still unclear. Robert et al. (1999) have realised the effect of the configuration OH – A – F, which leads to a new band due to a small shift of the A site cation towards the fluorine, having a higher electronegativity. This band only appears when the configuration of fluorine, filled A site and OH-group is given. While the configuration F – A – F does not produce any bands in the range  $3000\text{-}4000\text{ cm}^{-1}$ , the configuration OH – A – OH produces such peaks. The site configuration OH – □ – F also does not lead to any new bands since the fluorine does not influence the OH bonds directly.

In this study the peaks arising from OH bond stretching will be labeled in term of different chemical species of M1M1M3-OH-□ if A site adjacent to OH is vacant and M1M1M3-OH-A-W if the adjacent A site is occupied, with W = F or OH next to the A-site cation. For discussing the B/M4 site the nomenclature B-M1M1M3-OH is used. With Raman spectroscopy a distinguish of M1 and M3 is not possible. Therefore the order of Mg and Fe labelling the M1M1M3 peaks is not related to M1 or M3, but to M1/M3. Following this FeMgMg, MgFeMg and MgMgFe all label the same peak.

### 3.Results and discussion

#### 3.1. Electron microprobe analysis

During the data evaluation, first the measurements with too high (>102 wt-%) or too low (<95 wt-%) total weight% have been skipped, because they might represent surface defects or artificial signals. All measurements were always considered in detail before deciding to use them in the study. The totals of the oxide% of amphibole analysis depend on the content of OH<sup>-</sup> which cannot be measured by electron microprobe analysis, as well as on the F<sup>-</sup> or Cl<sup>-</sup> content, which are measurable but with relatively low accuracy. Therefore there is still a wide range of totals for good amphibole measurements. The scheme described in the IMA report appendix III on amphiboles of 2012 (IMA12, Hawthorne et al., 2012) has been applied to calculate the chemical formula of our amphiboles. The formula was calculated to 24 anions (O<sup>2-</sup> and 2(OH, F, Cl)) taking into account and (OH, F, Cl) = 2 - (2\*Ti) to estimate the O<sup>2-</sup> content on the W site. For each sample the chemical formula was recalculated assuming presence of Fe<sup>3+</sup> following the procedure (figure 8) described in the appendix III of IMA12. According to the procedure only samples a24, a27, a34, a35, a36, a38,

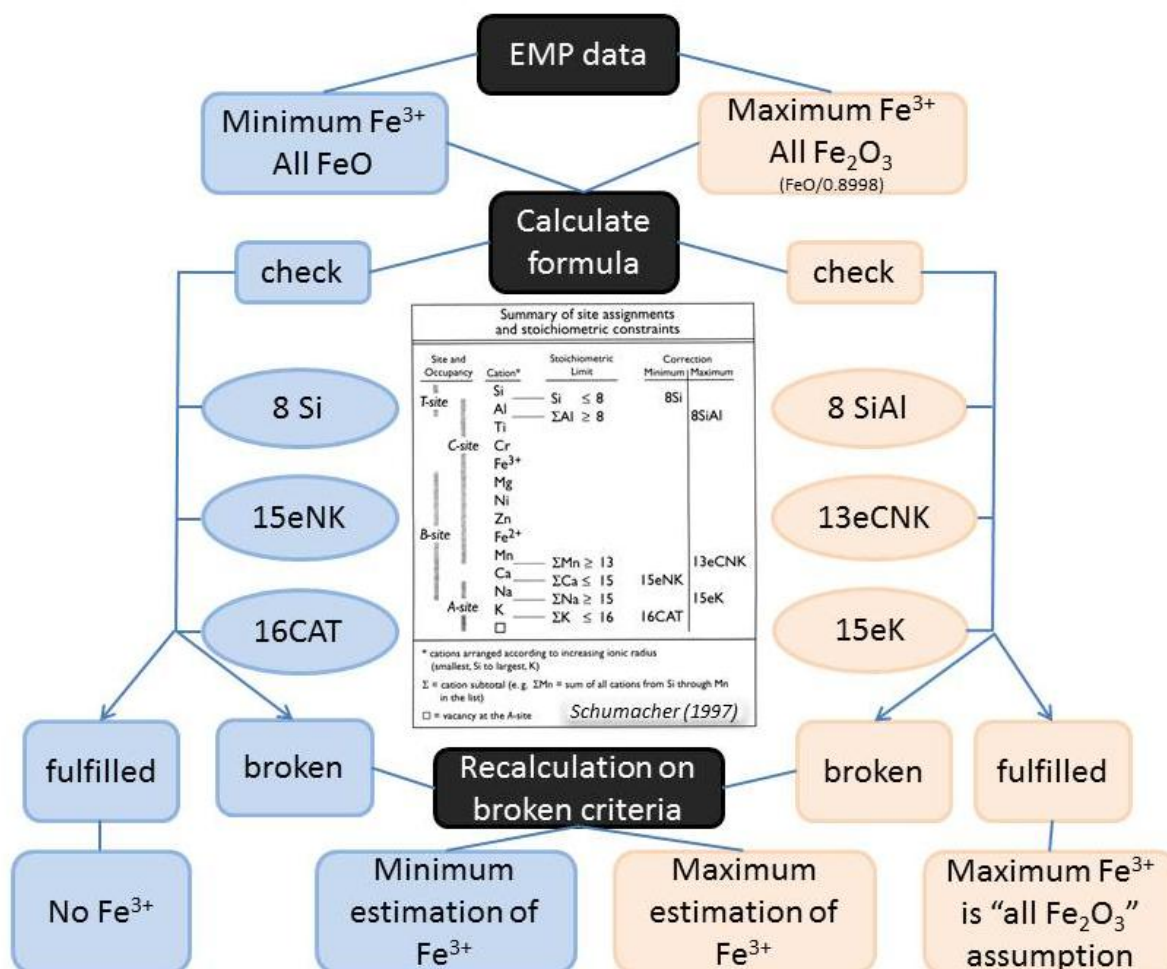


Figure 8: Simplified schema to estimate the Fe<sup>3+</sup> content, following the IMA report on amphiboles 2012 (Hawthorne et al., 2012) including the diagram of Schumacher (1997) in the center to describe the recalculate criteria.

a39, a40 and a42 show possible Fe<sup>3+</sup> content. For these samples recalculations were performed to estimate the Fe<sup>3+</sup> content. In doing so, at first the minimal and maximal Fe<sup>3+</sup> content have been calculated by assuming all iron as FeO and all iron as Fe<sub>2</sub>O<sub>3</sub>, respectively. Then the minimal Fe<sup>3+</sup> content (all iron as FeO-assumption) was used to calculate the other ion contents. The obtained ion contents were compared with the expected limitations on the amphibole crystal chemistry: the Si<sup>4+</sup> ions should be lower or equal to 8 (8Si) because of T<sub>8</sub> site in the primitive unit cell. Other cell structural criteria for the cation content are: all cations ≤ 16 (16CAT) and all cations without Na<sup>+</sup> and K<sup>+</sup> ≤ 15 (15eNK) (figure 8, centre). If all of these criteria are fulfilled there may be no Fe<sup>3+</sup> in the amphibole. This was true for the samples not mentioned above. If some of these criteria do not comply, there may be Fe<sup>3+</sup> and renormalization to the broken criteria has to be done. For example if 16CAT > 16, the ratio 16/(sum of all cations) is the renormalization coefficient for all cation contents. Via charge balance the possible Fe<sup>3+</sup> content can be now calculated, but has to be lower than the maximal Fe<sub>2</sub>O<sub>3</sub> content. If there are still more than one possible Fe<sup>3+</sup> contents, the best fitting has been chosen (Hawthorne et al., 2012). For samples a27, a28, a31, a33 and a36 the total weight sum and the recalculation show possible Li<sup>+</sup>. Therefore an estimation of Li<sup>+</sup> via the total weight% has been done to calculate the formula.

Following the scheme of Leake et al. (2003) the chemical formula was calculated. First the T-site was filled with Si<sup>4+</sup> and Al<sup>3+</sup> to 8. After that the rest Al<sup>3+</sup> goes on the C site followed by Ti<sup>4+</sup>, Fe<sup>3+</sup>, Cr<sup>3+</sup>, Mg<sup>2+</sup>, Fe<sup>2+</sup> and Mn<sup>2+</sup> to the limit of 5. Then the B site is filled with the remaining Mg<sup>2+</sup>, Fe<sup>2+</sup>, Mn<sup>2+</sup>, Ca<sup>2+</sup> and Na<sup>+</sup> until the total of 2 is reached. The remaining Ca<sup>2+</sup>, Na<sup>+</sup> and K<sup>+</sup> were then put on the A site. This filling-scheme is generally used, although natural samples may not behave alike and especially the Mg<sup>2+</sup> and Fe<sup>2+</sup> ions may vary over C and B site.

After calculating the formula, the correct amphibole name (after IMA12) was determined using the program AMPH2012 of Oberti et al. (2012) ([http://www\\_crystal.unipv.it/labcris/AMPH2012.zip](http://www_crystal.unipv.it/labcris/AMPH2012.zip)). The results are given in table 3. All samples have been supposed to be monoclinic. X-ray diffraction has only been performed on sample a7, which showed orthorhombic structure. Therefore this sample is not named cummingtonite but anthophyllite. For sample a42 the program exports the name “Ferri-No Name”. By reason of the high chemical similarity to sample a39 it is also named magnesio-arfvedsonite. In addition, the excel spreadsheet by Locock (2014) (<https://github.com/cageo/Locock-2013/releases>) has been applied. The results for the chemical formulae obtained by the above described procedure and the Locock-spreadsheet are almost the same. For some samples the resultant names are different. For example sample a39 and a42 were named magnesio-riebeckite by the Locock spreadsheet. Chemically both samples do not represent end members but rather intermediate composition of magnesio-riebeckite and magnesio-arfvedsonite, where denotation depends on whether the dominant A-site or C<sup>3+</sup>-site cation is used to determine the name. For this locality magnesio-arfvedsonite is confirmed ([www.mindat.org](http://www.mindat.org)) and therefore these samples were determined as magnesio-arfvedsonite. For sample a17 the Locock-spreadsheet gives the name cummingtonite, while the Oberti-program gives the name grunerite. Based on the Mg<sup>2+</sup> > Fe<sup>2+</sup> content the Locock-name fits better. Sample a10p, which is determined as richterite by the Oberti-program, in the Locock-spreadsheet is named ferri-winchite. This is due to different Fe<sup>3+</sup>-recalculations by the calculation schemes. The Fe<sup>3+</sup>-recalculation used by Oberti (2012) fits better to the Raman vs electron microprobe

analysis trend, therefore sample a10p is called richterite. The Locock-spreadsheet cannot calculate the  $\text{Li}^+$ -content as well as the  $\text{O}^{2-}$  content, hence the five samples with  $\text{Li}^+$  and the keasutite samples misleading nomenclature by the Locock-spreadsheet.

To compare the electron microprobe results with the Raman spectra, the  $\text{Mg}_C^*$  ( $\text{Mg}_C/(\text{Mg}_C+\text{Fe}^{2+}_C)$ ) ratio was determined. Because the calculating scheme of the formula is only a theoretical scheme, also the  $\text{Mg}_{\text{total}}^*$  ( $\text{Mg}_{\text{total}}/(\text{Mg}_{\text{total}}+\text{Fe}^{2+}_{\text{total}})$ ) has been calculated. Amphiboles with near or equal  $\text{Fe}^{2+}$  and  $\text{Mg}^{2+}$  contents shows different  $\text{Mg}_C^*$  and  $\text{Mg}_{\text{total}}^*$  ratios. Amphiboles with low  $\text{Mg}_B$  content do not show a major difference between these two ratios. For better comparison between electron microprobe analysis and Raman spectroscopy, where a specific determination between each cation is challenging,

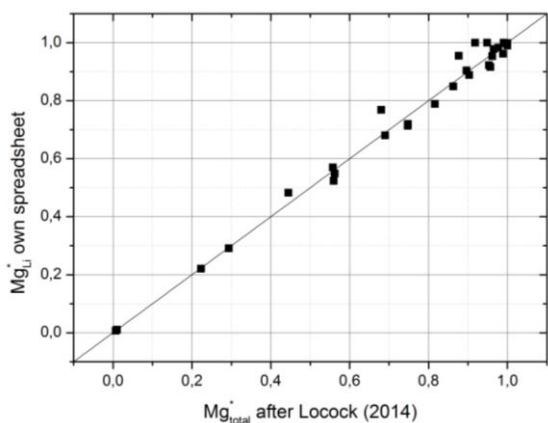


Figure 9: Comparison of  $\text{Mg}^*$ -calculated by using own Excel spreadsheet and the Spreadsheet of Locock (2014).

also the  $\text{Mg}_{\text{Li}}^*$  ( $\text{Mg}_{\text{total}}/(\text{Mg}_{\text{total}}+\text{Fe}^{2+}_{\text{total}}+\text{Li}_C)$ ) ratio was also calculated. Here an obvious change in the ratio appears only for amphiboles with  $\text{Li}_C$  content. The  $\text{Mg}_{\text{Li}}^*$  results from the above described formula calculation (own spreadsheet) is almost the same to the results obtained from the spreadsheet of Locock (2014). For the Locock-spreadsheet the  $\text{Mg}_{\text{total}}^*$  was calculated, because  $\text{Li}_C$  could not be estimated. Samples with  $\text{Li}^+$  have been neglected for this calculation. The Locock (2014) spreadsheet shows slightly lower  $\text{Mg}^*$  as compared to our own calculations, which can be seen in figure 9.

The electron microprobe results of a31 and a33 are ambiguous. Even with  $\text{Fe}^{3+}$ -recalculation and various estimations of  $\text{Li}^+$ , for a31 there are still more than three A- and B-site cations ( $\text{Na}^+$ ,  $\text{Ca}^{2+}$ ) and less than five C-site cations ( $\text{Fe}^{2+}$ ,  $\text{Fe}^{3+}$ ,  $\text{Mg}^{2+}$ ,  $\text{Al}^{3+}$ ,  $\text{Li}^+$ ). Single-crystal x-ray diffraction of a31 cannot solve the problem, neither to locate the excess amount of A- and B-site cations ( $\sim 3.5$  apfu  $\text{Na}^+$ ). Therefore it was not possible to name sample a31 up to now. Maybe additional Li-measurements can resolve this problem.

Table 3: Chemical composition of the studied samples, determined by electron microprobe analysis. Samples with assumed  $\text{Li}^+$  content (by total weight sum) are marked in red.

Sample	Name (IMA2012)	Chemistry
A4	Tremolite	$\text{Na}^{+}_{0,12} \text{A} (\text{Ca}^{2+}_{1,76} \text{Fe}^{2+}_{0,22} \text{Mn}^{2+}_{0,03}) \text{B} (\text{Mg}^{2+}_{4,54} \text{Fe}^{2+}_{0,35} \text{Al}^{3+}_{0,07} \text{Cr}^{3+}_{0,04}) \text{C} (\text{Al}^{3+}_{0,15} \text{Si}^{4+}_{7,85}) \text{T} \text{O}^{2-}_{22} (\text{OH}^{-}_{1,98} \text{F}^{-}_{0,02})$
A5	Tremolite	$(\text{Na}^{+}_{0,09} \text{Ca}^{2+}_{0,03}) \text{A} (\text{Ca}^{2+}_{1,83} \text{Mg}^{2+}_{0,14} \text{Mn}^{2+}_{0,02}) \text{B} \text{Mg}^{2+}_{5,00} \text{C} (\text{Al}^{3+}_{0,09} \text{Si}^{4+}_{7,90}) \text{T} \text{O}^{2-}_{22} (\text{OH}^{-}_{1,25} \text{F}^{-}_{0,75})$
A6	Tremolite	$(\text{Na}^{+}_{0,01} \text{Ca}^{2+}_{0,02}) \text{A} (\text{Ca}^{2+}_{1,87} \text{Mg}^{2+}_{0,08} \text{Mn}^{2+}_{0,03}) \text{B} \text{Mg}^{2+}_{5,00} \text{C} (\text{Al}^{3+}_{0,05} \text{Si}^{4+}_{7,95}) \text{T} \text{O}^{2-}_{22} (\text{OH}^{-}_{1,85} \text{F}^{-}_{0,15})$
A7	Anthophyllite	$(\text{Na}^{+}_{0,08} \text{Ca}^{2+}_{0,01}) \text{A} (\text{Mg}^{2+}_{1,87} \text{Fe}^{2+}_{0,11} \text{Ca}^{2+}_{0,01}) \text{B} (\text{Mg}^{2+}_{4,84} \text{Al}^{3+}_{0,16}) \text{C} (\text{Al}^{3+}_{0,27} \text{Si}^{4+}_{7,73}) \text{T} \text{O}^{2-}_{22} (\text{OH}^{-})_2$
A9	Grunerite	$(\text{Na}^{+}_{0,01} \text{Ca}^{2+}_{0,02}) \text{A} (\text{Fe}^{2+}_{1,77} \text{Mn}^{2+}_{0,19} \text{Ca}^{2+}_{0,03} \text{Zn}^{2+}_{0,01}) \text{B} (\text{Fe}^{2+}_{3,03} \text{Mg}^{2+}_{1,97} \text{Al}^{3+}_{0,01}) \text{C} (\text{Al}^{3+}_{0,04} \text{Si}^{4+}_{7,96}) \text{T} \text{O}^{2-}_{22} (\text{OH}^{-})_2$
A10	Tremolite	$(\text{Na}^{+}_{0,01} \text{Ca}^{2+}_{0,14}) \text{A} (\text{Ca}^{2+}_{1,83} \text{Mg}^{2+}_{0,12} \text{Fe}^{2+}_{0,05}) \text{B} \text{Mg}^{2+}_{5,00} \text{C} (\text{Al}^{3+}_{0,03} \text{Si}^{4+}_{7,92}) \text{T} \text{O}^{2-}_{22} (\text{OH}^{-})_2$
A10p	Richterite	$(\text{Na}^{+}_{0,32} \text{K}^{+}_{0,21}) \text{A} (\text{Ca}^{2+}_{1,27} \text{Na}^{+}_{0,54} \text{Fe}^{2+}_{0,17}) \text{B} (\text{Mg}^{2+}_{4,72} \text{Fe}^{2+}_{0,25} \text{Al}^{3+}_{0,02}) \text{C} (\text{Al}^{3+}_{0,02} \text{Si}^{4+}_{7,98}) \text{T} \text{O}^{2-}_{22} (\text{OH}^{-}_{1,73} \text{F}^{-}_{0,27})$
A12	Pargasite	$(\text{Na}^{+}_{0,63} \text{K}^{+}_{0,10}) \text{A} (\text{Ca}^{2+}_{1,75} \text{Fe}^{2+}_{0,20} \text{Mn}^{2+}_{0,04} \text{Na}^{+}_{0,01}) \text{B} (\text{Mg}^{2+}_{2,06} \text{Fe}^{2+}_{2,00} \text{Al}^{3+}_{0,89} \text{Ti}^{4+}_{0,05}) \text{C} (\text{Al}^{3+}_{1,74} \text{Si}^{4+}_{6,26}) \text{T} \text{O}^{2-}_{22} (\text{OH}^{-}_{1,98} \text{F}^{-}_{0,01} \text{Cl}^{-}_{0,01})$
A13	Glaucofane	$(\text{Na}^{+}_{0,08} \text{K}^{+}_{0,01}) \text{A} (\text{Na}^{+}_{1,74} \text{Ca}^{2+}_{0,11} \text{Fe}^{2+}_{0,14} \text{Mn}^{2+}_{0,01}) \text{B} (\text{Mg}^{2+}_{2,69} \text{Al}^{3+}_{1,68} \text{Fe}^{2+}_{0,59}) \text{C} (\text{Al}^{3+}_{0,06} \text{Si}^{4+}_{7,94}) \text{T} \text{O}^{2-}_{22} (\text{OH}^{-}_{1,96} \text{F}^{-}_{0,04})$
A15	Richterite	$(\text{Na}^{+}_{0,35} \text{K}^{+}_{0,23}) \text{A} (\text{Ca}^{2+}_{1,17} \text{Na}^{+}_{0,62} \text{Fe}^{2+}_{0,17} \text{Mn}^{2+}_{0,03} \text{Sr}^{2+}_{0,02}) \text{B} (\text{Mg}^{2+}_{3,62} \text{Fe}^{2+}_{1,28} \text{Al}^{3+}_{0,07} \text{Ti}^{4+}_{0,02}) \text{C} (\text{Al}^{3+}_{0,22} \text{Si}^{4+}_{7,78}) \text{T} \text{O}^{2-}_{22} (\text{OH}^{-}_{1,85} \text{F}^{-}_{0,15})$
A16	Grunerite	$(\text{K}^{+}_{0,02} \text{Ca}^{2+}_{0,02}) \text{A} (\text{Fe}^{2+}_{1,53} \text{Mn}^{2+}_{0,50}) \text{B} (\text{Fe}^{2+}_{3,56} \text{Mg}^{2+}_{1,44}) \text{C} (\text{Al}^{3+}_{0,03} \text{Si}^{4+}_{7,96}) \text{T} \text{O}^{2-}_{22} (\text{OH}^{-})_2$
A17	Grunerite	$(\text{Na}^{+}_{0,02} \text{Ca}^{2+}_{0,03}) \text{A} (\text{Fe}^{2+}_{0,97} \text{Mn}^{2+}_{0,89} \text{Ca}^{2+}_{0,13}) \text{B} (\text{Fe}^{2+}_{1,71} \text{Mg}^{2+}_{3,26}) \text{C} (\text{Al}^{3+}_{0,12} \text{Si}^{4+}_{7,88}) \text{T} \text{O}^{2-}_{22} (\text{OH}^{-}_{1,98} \text{F}^{-}_{0,01} \text{Cl}^{-}_{0,01} \text{O}^{2-}_{0,01})$
A18	Tremolite	$(\text{Na}^{+}_{0,09} \text{K}^{+}_{0,01}) \text{A} (\text{Ca}^{2+}_{1,69} \text{Fe}^{2+}_{0,21} \text{Mn}^{2+}_{0,02}) \text{B} (\text{Mg}^{2+}_{4,47} \text{Fe}^{2+}_{0,47} \text{Cr}^{3+}_{0,03}) \text{C} (\text{Al}^{3+}_{0,36} \text{Si}^{4+}_{7,64}) \text{T} \text{O}^{2-}_{22} (\text{OH}^{-}_{1,98} \text{F}^{-}_{0,02})$
A19	Actinolite	$(\text{Na}^{+}_{0,16} \text{K}^{+}_{0,01}) \text{A} (\text{Ca}^{2+}_{1,74} \text{Fe}^{2+}_{0,24} \text{Mn}^{2+}_{0,02}) \text{B} (\text{Mg}^{2+}_{4,33} \text{Fe}^{2+}_{0,53} \text{Al}^{3+}_{0,1} \text{Cr}^{3+}_{0,05}) \text{C} (\text{Al}^{3+}_{0,18} \text{Si}^{4+}_{7,82}) \text{T} \text{O}^{2-}_{22} (\text{OH}^{-}_{1,99} \text{F}^{-}_{0,01})$
A21	Tremolite	$(\text{Na}^{+}_{0,07} \text{K}^{+}_{0,01}) \text{A} (\text{Ca}^{2+}_{1,81} \text{Fe}^{2+}_{0,11} \text{Mg}^{2+}_{0,08}) \text{B} (\text{Mg}^{2+}_{4,84} \text{Al}^{3+}_{0,16}) \text{C} (\text{Al}^{3+}_{0,23} \text{Si}^{4+}_{7,77}) \text{T} \text{O}^{2-}_{22} (\text{OH}^{-}_{1,87} \text{F}^{-}_{0,13})$
A23	Cummingtonite	$(\text{Ca}_{0,07} \text{Na}^{+}_{0,03} \text{K}^{+}_{0,01}) \text{A} (\text{Fe}^{2+}_{1,96} \text{Mn}^{2+}_{0,04} \text{Ca}^{2+}_{0,01}) \text{B} (\text{Mg}^{2+}_{4,99} \text{Ti}^{4+}_{0,01}) \text{C} (\text{Al}^{3+}_{0,09} \text{Si}^{4+}_{7,86}) \text{T} \text{O}^{2-}_{22} (\text{OH}^{-})_2$
A24	Ferri-kaersutite	$(\text{Na}^{+}_{0,51} \text{K}^{+}_{0,36}) \text{A} (\text{Ca}^{2+}_{1,77} \text{Na}^{+}_{0,14} \text{Mg}^{2+}_{0,07} \text{Ba}^{2+}_{0,01} \text{Mn}^{2+}_{0,01}) \text{B} (\text{Mg}^{2+}_{3,01} \text{Fe}^{3+}_{1,03} \text{Al}^{3+}_{0,30} \text{Ti}^{4+}_{0,66}) \text{C} (\text{Si}^{4+}_{5,84} \text{Al}^{3+}_{2,16}) \text{T} \text{O}^{2-}_{22} (\text{OH}^{-}_{0,64} \text{F}^{-}_{0,06} \text{O}^{2-}_{1,32})$
A25	Cummingtonite	$(\text{Na}^{+}_{0,32}) \text{A} (\text{Mg}^{2+}_{1,68} \text{Fe}^{2+}_{0,28} \text{Na}^{+}_{0,01} \text{Ca}^{2+}_{0,03}) \text{B} (\text{Mg}^{2+}_{4,21} \text{Al}^{3+}_{0,77} \text{Ti}^{4+}_{0,02}) \text{C} (\text{Al}^{3+}_{1,13} \text{Si}^{4+}_{6,88}) \text{T} \text{O}^{2-}_{22} (\text{OH}^{-}_{1,98} \text{F}^{-}_{0,02} \text{Cl}^{-}_{0,01})$
A26	Tremolite	$(\text{Na}^{+}_{0,01} \text{Ca}_{0,04}) \text{A} (\text{Ca}^{2+}_{1,80} \text{Fe}^{2+}_{0,06} \text{Mn}^{2+}_{0,14}) \text{B} (\text{Mg}^{2+}_{4,87} \text{Fe}^{2+}_{0,13}) \text{C} (\text{Al}^{3+}_{0,04} \text{Si}^{4+}_{7,90}) \text{T} \text{O}^{2-}_{22} (\text{OH}^{-}_{1,74} \text{F}^{-}_{0,26})$
A27	Clino-holmquistite	$\text{Na}^{+}_{0,02} \text{A} (\text{Li}^{+}_{1,96} \text{Fe}^{2+}_{0,04}) \text{B} (\text{Mg}^{2+}_{2,55} \text{Fe}^{2+}_{0,726} \text{Fe}^{3+}_{0,43} \text{Al}^{3+}_{1,30} \text{Mn}^{2+}_{0,02} \text{Zn}^{2+}_{0,01}) \text{C} (\text{Al}^{3+}_{0,26} \text{Si}^{4+}_{7,74}) \text{T} \text{O}^{2-}_{22} (\text{OH}^{-}_{1,98} \text{F}^{-}_{0,02})$
A28	Clino-ferro-holmquistite	$(\text{Li}^{+}_{1,80} \text{Na}^{+}_{0,04} \text{Fe}^{2+}_{0,13} \text{Mn}^{2+}_{0,02}) \text{B} (\text{Mg}^{2+}_{1,34} \text{Fe}^{2+}_{1,69} \text{Al}^{3+}_{1,97}) \text{C} (\text{Al}^{3+}_{0,13} \text{Si}^{4+}_{7,87}) \text{T} \text{O}^{2-}_{22} (\text{OH}^{-})_2$
A29	Fluoro-edenite	$(\text{Na}^{+}_{0,41} \text{K}^{+}_{0,22}) \text{A} (\text{Ca}^{2+}_{1,54} \text{Na}^{+}_{0,44} \text{Mn}^{2+}_{0,02}) \text{B} (\text{Mg}^{2+}_{4,70} \text{Fe}^{2+}_{0,23} \text{Ti}^{4+}_{0,01}) \text{C} (\text{Al}^{3+}_{0,29} \text{Si}^{4+}_{7,57}) \text{T} \text{O}^{2-}_{22} (\text{OH}^{-}_{0,84} \text{F}^{-}_{1,16})$

A30	Richterite	$(\text{Na}^+_{0,59}\text{K}^+_{0,33})^A(\text{Ca}^{2+}_{1,14}\text{Na}^+_{0,86})^B(\text{Mg}^{2+}_{4,91}\text{Fe}^{2+}_{0,01}\text{Ti}^{4+}_{0,01})^C(\text{Al}^{3+}_{0,28}\text{Si}^{4+}_{7,67})^T\text{O}^{2-}_{22}(\text{OH}^-_{1,51}\text{F}^-_{0,48})$
A31		$(\text{Na}^+_{1,99}\text{K}^+_{0,03})^A(\text{Na}^+_{1,59}\text{Ca}^{2+}_{0,41})^B(\text{Li}^+_{0,86}\text{Fe}^{2+}_{3,42}\text{Al}^{3+}_{0,42}\text{Mg}^{2+}_{0,16}\text{Mn}^{2+}_{0,03}\text{Ti}^{4+}_{0,03})^C(\text{Si}^{4+}_{7,99}\text{Al}^{3+}_{0,01})^T\text{O}^{2-}_{22}(\text{OH}^-_{1,78}\text{F}^-_{0,15}\text{O}^{2-}_{0,06})$
A33	Ferri-fluoro-leakeite	$(\text{Na}^+_{0,61}\text{K}^+_{0,42})^A(\text{Na}^+_{1,89}\text{Ca}^{2+}_{0,03})^B(\text{Li}^+_{1,53}\text{Fe}^{3+}_{1,77}\text{Mg}^{2+}_{1,68}\text{Zn}^{2+}_{0,05})^C(\text{Al}^{3+}_{0,32}\text{Si}^{4+}_{7,58}\text{Ti}^{4+}_{0,1})^T\text{O}^{2-}_{22}(\text{OH}^-_{0,56}\text{F}^-_{1,1}\text{O}^{2-}_{0,19})$
A34	Arfvedsonite	$(\text{Na}^+_{0,64}\text{K}^+_{0,34})^A(\text{Na}^+_{1,74}\text{Ca}^{2+}_{0,26})^B(\text{Fe}^{2+}_{3,79}\text{Fe}^{3+}_{0,94}\text{Mg}^{2+}_{0,04}\text{Mn}^{2+}_{0,08}\text{Ti}^{4+}_{0,07}\text{Zn}^{2+}_{0,01})^C(\text{Al}^{3+}_{0,50}\text{Si}^{4+}_{7,50})^T\text{O}^{2-}_{22}(\text{OH}^-_{1,34}\text{F}^-_{0,51}\text{O}^{2-}_{0,15})$
A35	Arfvedsonite	$(\text{Na}^+_{0,65}\text{K}^+_{0,36})^A(\text{Na}^+_{1,55}\text{Ca}^{2+}_{0,44}\text{Mn}^{2+}_{0,01})^B(\text{Fe}^{2+}_{4,14}\text{Fe}^{3+}_{0,72}\text{Mg}^{2+}_{0,03}\text{Ti}^{4+}_{0,07}\text{Mn}^{2+}_{0,06}\text{Zn}^{2+}_{0,01})^C(\text{Al}^{3+}_{0,51}\text{Si}^{4+}_{7,47})^T\text{O}^{2-}_{22}(\text{OH}^-_{1,42}\text{F}^-_{0,52}\text{O}^{2-}_{0,14})$
A36	Potassic-ferri-leakeite	$(\text{Na}^+_{0,06}\text{K}^+_{0,42})^A(\text{Na}^+_{1,39}\text{Mn}^{2+}_{0,47}\text{Li}^+_{0,14})^B(\text{Li}^+_{1,02}\text{Fe}^{3+}_{1,56}\text{Mg}^{2+}_{2,19}\text{Al}^{3+}_{0,11}\text{Ti}^{4+}_{0,06})^C\text{Si}^{4+}_8\text{O}^{2-}_{22}(\text{OH}^-_{1,13}\text{F}^-_{0,74}\text{O}^{2-}_{0,12})$
A37	Tremolite	$(\text{Na}^+_{0,33}\text{K}^+_{0,12})^A(\text{Ca}^{2+}_{1,45}\text{Na}^+_{0,47}\text{Mn}^{2+}_{0,07}\text{Fe}_{0,01})^B(\text{Mg}^{2+}_{4,55}\text{Fe}^{2+}_{0,38}\text{Al}^{3+}_{0,06})^C(\text{Al}^{3+}_{0,28}\text{Si}^{4+}_{7,72})^T\text{O}^{2-}_{22}(\text{OH}^-_{1,72}\text{F}^-_{0,28})$
A38	Arfvedsonite	$(\text{Na}^+_{0,46}\text{K}^+_{0,22})^A(\text{Na}^+_{1,90}\text{Ca}^{2+}_{0,02}\text{Mn}^{2+}_{0,07})^B(\text{Fe}^{2+}_{3,64}\text{Fe}^{3+}_{0,96}\text{Al}^{3+}_{0,20}\text{Mn}^{2+}_{0,1}\text{Mg}^{2+}_{0,01}\text{Zn}^{2+}_{0,06}\text{Ti}^{4+}_{0,04})^C(\text{Si}^{4+}_{8,0})^T\text{O}^{2-}_{22}(\text{OH}^-_{1,03}\text{F}^-_{0,89}\text{O}^{2-}_{0,07})$
A39	Magnesio-arfvedsonite	$(\text{Na}^+_{0,35}\text{K}^+_{0,17})^A(\text{Na}^+_{1,60}\text{Ca}^{2+}_{0,31}\text{Mn}^{2+}_{0,09})^B(\text{Mg}^{2+}_{3,62}\text{Fe}^{3+}_{1,22}\text{Al}^{3+}_{0,09}\text{Ti}^{4+}_{0,01})^C(\text{Si}_{7,83}\text{Al}^{3+}_{0,17})^T\text{O}^{2-}_{22}(\text{OH}^-_{1,63}\text{F}^-_{0,35})$
A40	Ferri-kaersutite	$(\text{Na}^+_{0,73}\text{K}^+_{0,18})^A(\text{Ca}^{2+}_{1,98}\text{Mn}^{2+}_{0,02})^B(\text{Mg}^{2+}_{2,98}\text{Fe}^{3+}_{0,45}\text{Al}^{3+}_{0,11}\text{Ti}^{4+}_{0,78}\text{Fe}^{2+}_{0,78})^C(\text{Si}^{4+}_{5,85}\text{Al}^{3+}_{2,15})^T\text{O}^{2-}_{22}(\text{OH}^-_{0,34}\text{O}^{2-}_{1,53}\text{Cl}^-_{0,09})$
A41	Magnesio-hornblende	$(\text{Na}^+_{0,45}\text{K}^+_{0,04})^A(\text{Ca}^{2+}_{1,74}\text{Na}^+_{0,02}\text{Fe}^{2+}_{0,20}\text{Mn}^{2+}_{0,03})^B(\text{Mg}^{2+}_{2,61}\text{Fe}^{2+}_{1,78}\text{Al}^{3+}_{0,59}\text{Ti}^{4+}_{0,02})^C(\text{Al}^{3+}_{1,09}\text{Si}^{4+}_{6,91})^T\text{O}^{2-}_{22}(\text{OH}^-_{1,99}\text{F}^-_{0,01}\text{O}^{2-}_{0,05})$
A42	Magnesio-arfvedsonite	$(\text{Na}^+_{0,25}\text{K}^+_{0,13})^A(\text{Na}^+_{1,77}\text{Ca}^{2+}_{0,23})^B(\text{Mg}^{2+}_{3,51}\text{Fe}^{3+}_{1,30}\text{Al}^{3+}_{0,04}\text{Mn}^{2+}_{0,05})^C(\text{Si}^{4+}_{7,94}\text{Al}^{3+}_{0,06})^T\text{O}^{2-}_{22}(\text{OH}^-_{1,70}\text{F}^-_{0,30})$



## 3.2. Raman spectroscopy

Raman spectra were measured in four configurations: sample vertical in the visible field of optical

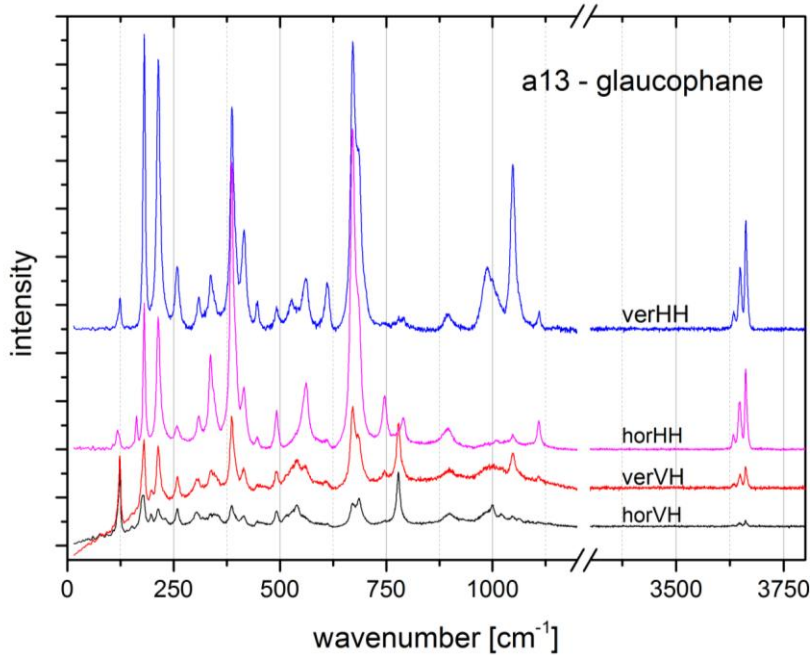


Figure 10: Raman spectra of glaucophane sample (a13) measured in four experimental configurations.

microscope, with parallel polarized light (verHH), sample vertical with cross polarized light (verVH) (figure 5, left site), sample horizontal with parallel polarized light (horHH) and sample horizontal with cross polarized light (horVH) (figure 5, right site). The best spectra were achieved with parallel polarized light; the cross polarized spectra always show lower intensities. Some samples do not show any OH-stretching modes in the cross polarized orientations or the corresponding peaks are too low to be evaluated. Differences in vertical vs. horizontal orientation of the sample are seen in the lower part of the spectra. A typical intensity distribution of the orientations is shown in figure 10. The different polarization behaviour is due to the difference in the components of the polarizability tensor (figure 6). While verHH and horHH with parallel polarization show two different tensor components of the  $A_g$  modes, verVH and horVH show the same component of the  $A_g$  mode components (or depending on the orientation of the needle of the crystal, what is discussed later, the same component of the  $B_g$  mode).

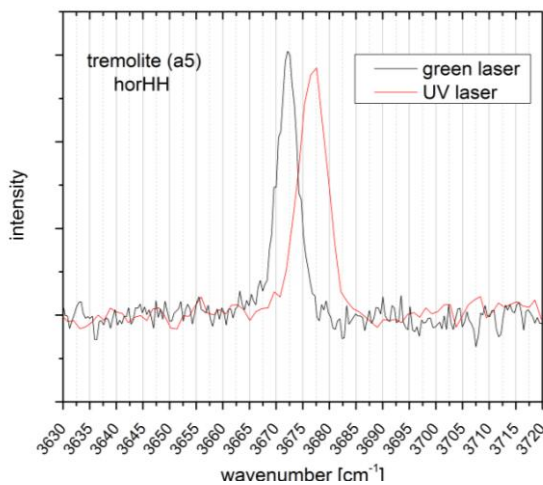


Figure 11: Slight mismatch of the Raman peak position due to the use of visible or UV laser.

microscope, with parallel polarized light (verHH), sample vertical with cross polarized light (verVH) (figure 5, left site), sample horizontal with parallel polarized light (horHH) and sample horizontal with cross polarized light (horVH) (figure 5, right site). The best spectra were achieved with parallel polarized light; the cross polarized spectra always show lower intensities. Some samples do not show any OH-stretching modes in the cross polarized orientations or the corresponding

peaks are too low to be evaluated. Differences in vertical vs. horizontal orientation of the sample are seen in the lower part of the spectra. A typical intensity distribution of the orientations is shown in figure 10. The different polarization behaviour is due to the difference in the components of the polarizability tensor (figure 6). While verHH and horHH with parallel polarization show two different tensor components of the  $A_g$  modes, verVH and horVH show the same component of the  $A_g$  mode components (or depending on the orientation of the needle of the crystal, what is discussed later, the same component of the  $B_g$  mode).

$$\frac{verHH + horHH}{2}$$

For evaluating the spectra the average of the parallel polarized configurations has been used. This has been calculated with:

Orientations verVH and horVH have been neglected, because they always had low intensities and low-quality spectra. In Porto notation the verHH orientation represents  $\bar{y}(x'x')y$  orientation, while horHH represents  $\bar{y}(zz)y$ , verVH shows  $\bar{y}(x'z)y$  and horVH is  $\bar{y}(zx')y$ , where  $z$  is along the monoclinic  $c$  axis,  $y$  is along the monoclinic  $b$  axis, while  $x'$  is perpendicular  $\alpha$  the  $(b,c)$  plane ( $C2/m$  setting with unique  $b$  axis)

Sample a5 have been measured with green and UV laser, so that it is possible to check the changes due to the different lasers. By comparing the OH-spectra of the different lasers in figure 11, a shift of ca.  $3\text{ cm}^{-1}$  to higher frequencies can be seen due to the unavoidable difference in the procedure of spectrometer alignment: to the Si peaks at  $520.5\text{ cm}^{-1}$  for visible configuration and to the diamond peak at  $1332\text{ cm}^{-1}$  for the UV configuration This has to be taken into account, when comparing the spectra.

### 3.2.1. Spectral range of skeleton vibrations ( $15 - 1215\text{ cm}^{-1}$ )

As expected, all spectra show the strong  $\text{SiO}_4$ -breathing mode around  $650\text{--}700\text{ cm}^{-1}$ . On the basis of the bands around  $900\text{--}1100\text{ cm}^{-1}$  the samples can be separated into two groups. One group shows a huge difference in these peaks between the verHH and the horHH orientation. The other group, do not show such a difference. For example, in figure 12 (top) there are samples a13 and a19. Sample a13 exhibits a change in the peak intensities in the range  $900\text{--}1100\text{ cm}^{-1}$ , which is dominated by  $\text{Si-O}_{\text{non-bridging}}$  vibrations. Sample a19 does not show such strong polarization-depending peaks. This is

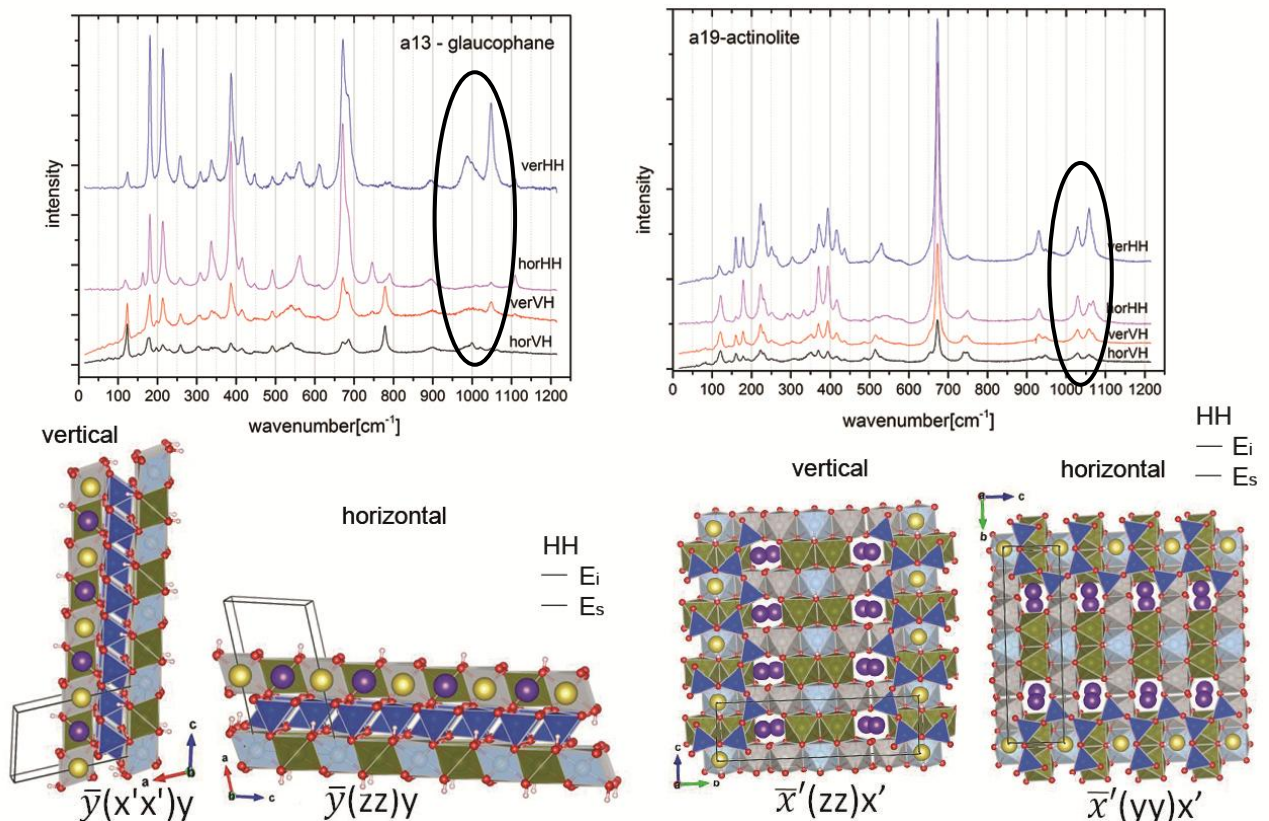


Figure 12: **Top:** Raman spectra in the range of  $15\text{--}1215\text{ cm}^{-1}$ . On the left hand site, the spectra of glaucophane, show strong orientation dependence of the peak intensity in the range of  $900\text{--}1100\text{ cm}^{-1}$ , arising from the  $\text{Si-O}_{\text{non-bridging}}$  stretching mode. On the right hand site, the spectra of actinolite do not exhibit such dependence. **Bottom:** Macroscopically labeled horizontal/vertical orientation can mean two different orientations from structural view due to uncertainties in the orientation of the  $b$  axis. On the left-hand side the polarization of the incident and scattering light is in the  $(a\text{--}c)$  plane and the atomic vector displacement for the  $\text{Si-O}_{\text{non-bridging}}$  stretching mode are either approximately parallel (vertical orientation) or perpendicular (horizontal orientation) to polarization of the incident light  $E_i$  and scattering light  $E_s$ . On the right-hand side is the photon polarization in the  $(b\text{--}c)$ -plane, and atomic displacement vectors for  $\text{Si-O}_{\text{non-bridging}}$  stretching mode are  $\perp E_i$  and  $E_s$ , in both vertical and horizontal orientation; hence the intensity is weakly dependent on the orientation.

due to the fact that the amphibole needles can have two horizontal orientations and hence two different orientations of the Si-O<sub>bridging</sub> bond and Si-O<sub>non-bridging</sub> with respect to the polarization of the incident and scattered photon. In one group of samples the laser propagation was  $\perp$  to the  $(a,b)$  plane and therefore the polarization of both the incident and scattered photons were in the plane of Si-O rings. For the other samples where measured with the laser propagating along the  $b$  axis and thus the SiO<sub>4</sub>-ring vibrations were measured from aside (figure 12; bottom). Given that the light is always polarized, the measurement on  $(a,c)$  plane spots the change of the orientation of SiO<sub>4</sub>-ring. This is also the reason for the orientation-depending intensities of the peaks.

### 3.2.2. OH-bond stretching mode (3400 - 3800 cm<sup>-1</sup>)

All Raman spectra in the range from 2600 to 3800 cm<sup>-1</sup> were baseline corrected to eliminate photoluminescence effects. All baseline corrected Raman spectra of the OH band stretching modes of the studied amphiboles can be seen in the appendix. After this all peaks were fitted with pseudo-Voigt functions. The pseudo-Voigt function is a sum of a Lorentzian and Gaussian peak-shape function. The Lorentzian function represents homogeneous broadening, while the Gaussian function represents the inhomogeneous broadening due to the statistical distribution, e.g. chemical disorder, which is expected in the spectra of amphiboles. Then the peaks were related to different Mg<sup>2+</sup>-Fe<sup>2+</sup> chemical environments on the triplet of M1M1M3 sites (MgMgMg-OH-□, MgMgFe-OH-□, MgFeFe-OH-□, FeFeFe-OH-□) and the Raman peak intensities were compared to the chemical composition of the corresponding amphibole sample. Samples with only <sup>C</sup>Mg<sup>2+</sup> (e.g. tremolite a10) possess one strong peak at wavenumber about 3660 to 3674 cm<sup>-1</sup>, whereas sample with intermediate <sup>C</sup>Fe<sup>2+</sup>-<sup>C</sup>Mg<sup>2+</sup> composition show up to four peaks. With <sup>C</sup>Fe<sup>2+</sup>-content increase, peaks at lower frequencies are enhanced, while with higher <sup>C</sup>Mg<sup>2+</sup>-content the peaks with higher frequencies gets stronger. Thereby peaks have been related to the Mg<sup>2+</sup>-Fe<sup>2+</sup> content on M1- and M3-site. Figure 13 illustrates a grunerite sample (a9), which shows four OH peaks and has an intermediate composition of <sup>C</sup>Fe<sup>2+</sup> 3.03 apfu and <sup>C</sup>Mg<sup>2+</sup> 1.97 apfu. As expected from infrared spectroscopy, the FeFeFe-OH-□ peak appears at a lower

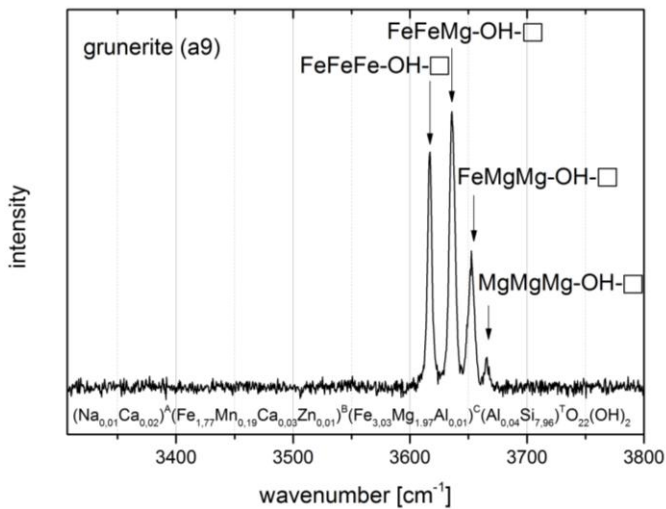


Figure 13: Raman scattering of grunerite (a9) originating from OH-stretching modes.

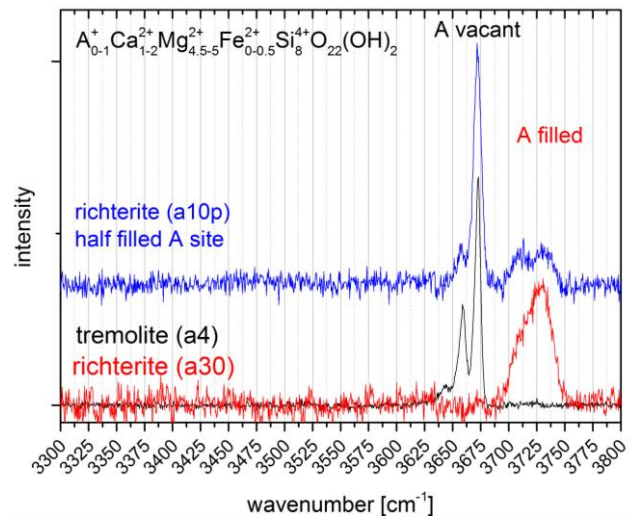


Figure 14: Raman scattering of tremolite and richterite generated by OH-stretching modes. The peak shift of ca. 55 cm<sup>-1</sup> is due to the A-site occupancies.

wavenumber than the MgMgMg-OH-□ peak and the intermediate FeFeMg-OH-□ and FeMgMg-OH-□ peaks appear between them. Samples with partially filled A site exhibit a broad Raman band at higher frequencies. This band can be related to the occupation of the A site, which compresses the OH bonds and therefore should appear at higher frequencies. While samples with partially filled A site show both narrow lower-wavenumber and broad higher-wavenumber peaks, samples with completely filled A site show only higher-wavenumber peaks. Similar to infrared spectroscopic data, the Raman spectra show the same shift of about 50-60 cm<sup>-1</sup> towards higher frequencies related with a filled A-site. In Figure 14 this can be seen for two richterite and one tremolite samples; the two broad peaks of sample a10p are discussed later in detail (figure 25).

Using the fractional intensities of peaks attributed to chemically different M1M1M3 species, the Raman-Mg\* ratio had been calculated with:

$$Mg^*_{Raman} = \frac{3I_{MMM} + 2I_{FMM} + I_{FFM}}{3I_{MMM} + 3I_{FMM} + 3I_{FFM} + 3I_{FFF}}$$

where I<sub>MMM</sub> is the fractional intensity of the MgMgMg-OH peak (in the range of 3664 to 3674 cm<sup>-1</sup> for MgMgMg-OH-□ and 3715 to 3730 cm<sup>-1</sup> for MgMgMg-OH-A), I<sub>MMF</sub> is the normalized intensity of MgMgFe-peak (in the range of 3650 to 3661 cm<sup>-1</sup> for MMgFe-OH-□ and 3700 to 3711 cm<sup>-1</sup> for MgMgFe-OH-A), etc. Similar calculations of Mg<sup>2+</sup>- and Fe<sup>2+</sup>-content have been used by Burns & Strens (1966) for infrared spectra and Chen et al. (2004) for Raman spectra.

The Mg\*<sub>Raman</sub> ratio was compared with the Mg\* ratios derived from electron microprobe analysis. While the Mg<sub>C</sub>\* ratio (Mg<sub>C</sub>/(Fe<sub>C</sub>+Mg<sub>C</sub>)) always shows higher values than that calculated from the Raman spectra, the Mg<sub>Li</sub>\* (Mg<sub>total</sub>/(Mg<sub>total</sub>+Fe<sup>2+</sup><sub>total</sub>+Li<sub>C</sub>)) ratio matches quite well the Mg\*<sub>Raman</sub> ratio,

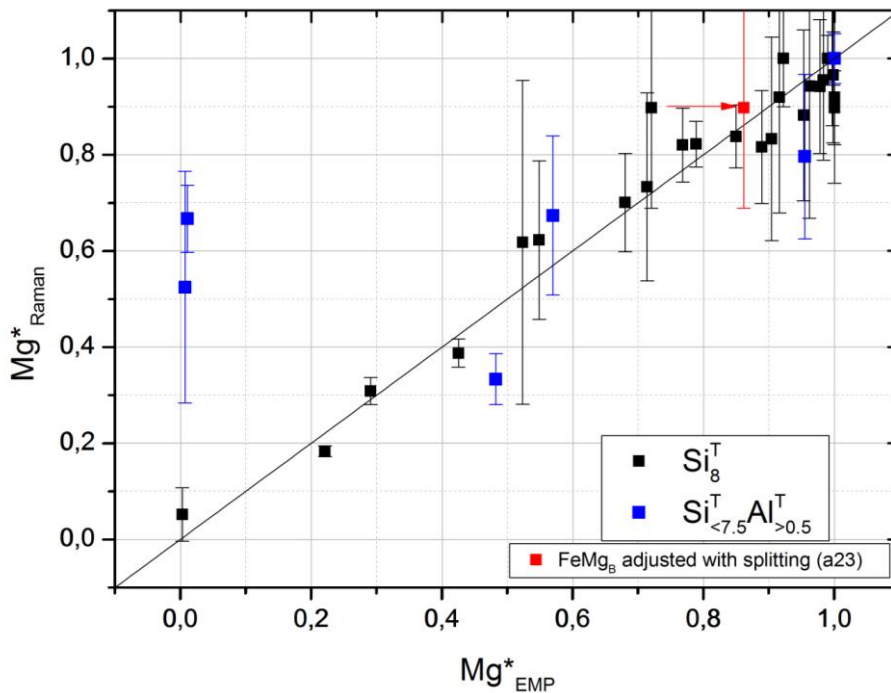


Figure 15: Mg\*-ratio, calculated from the Raman spectroscopic data versus the ratio calculated from electron microprobe analysis (Mg<sub>Li</sub>\*). The red data point is obtained after taking into account possible Mg/Fe distribution on the B site.

where Li<sub>C</sub> is calculated from EMP data at the basis of the total weigh sum. This is presented in figure 15.

Compared to the electron microprobe analysis the M1M1M3 site composition can be analysed more accurate with Raman spectroscopy. In figure 16 three samples with nearly similar Raman

spectra of the OH bond stretching mode can be seen. The peaks indicate a quite same M1M1M3-composition for all three samples (a4, a18 and a19) whereas the calculation based on electron microprobe analysis show difference in  ${}^C\text{Fe}^{2+}$ , especially of sample a4 and a19. Based on the calculation scheme for electron microprobe analysis all three samples also contain  ${}^B\text{Fe}^{2+}$ . While the electron microprobe analysis can only determine the total Fe content, Raman spectroscopy can also determine the Fe-Mg composition of C site. Related to figure 16 the Raman spectra of a4 shows that the  $\text{Fe}^{2+}$  content at C site must be higher than calculated based on electron microprobe analysis data and the calculation scheme. The difference of tremolite and actinolite is the  ${}^C\text{Fe}^{2+}$  content. If the  ${}^C\text{Fe}^{2+}$  is higher than 0.5 apfu the sample is names actinolite. Due to the similar Raman spectra sample a4 and a18 maybe also are actinolites instead of tremolites. Therefore Raman spectroscopy can lead to a better classification of the amphiboles.

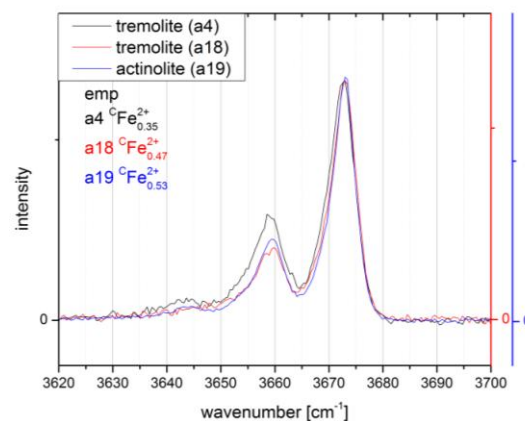


Figure 16: The OH stretching modes of tremolite (a4, a18) and actinolite (a19) sample show better  ${}^C\text{Fe}^{2+}$  determination than the calculation scheme of electron microprobe analysis

Some samples, in particular the cummingtonite samples (a23, a7, a25), show subtle splitting of all M1M1M3 peaks related to vacant A site (figure 17 shows this for samples a23). On an enlarged scale

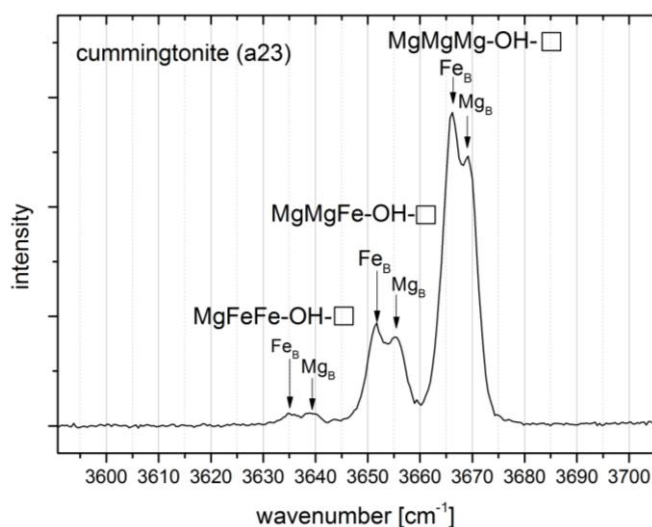


Figure 17: Raman scattering of cummingtonite (a23) caused by OH-stretching modes.

one can also notice that the peak attributed to  $\text{MgMgMg-OH-}\square$  vary in the range from 3660 to 3675  $\text{cm}^{-1}$ , depending on the sample. This makes the determination of specific samples to specific configurations challenging. It is not obvious what effect is responsible for the small shifts. On the one hand, the configuration of C-site cations on M2 site may have indirect influence on the OH stretching. On the other hand, the B-site cations may also have a small effect on the OH-peak positions, through their influence on the  $\text{SiO}_4$ -ring geometry, which would slightly affect the void available for OH

bond stretching vibrations. If there is a trivalent cation ( $\text{Al}^{3+}$ ,  $\text{Fe}^{3+}$ ) on M1 and/or M3 sites, that may lead to a shift of the Raman OH-peak. This shift is similar in nature to the effect of  $\text{Fe}^{2+}$  but it should be larger because the degree of covalency of the Al-O bond is larger than that of the Fe-O bond. But in this study no peaks arising from trivalent cations at M1/M3 site have been identified.

The B-site should not have a strong effect on the OH-stretching mode. However the influence of B-site or M2-site chemistry cannot be neglected and therefore this could be the reason for splitting. Following the idea of B-site influence, the normalized intensities of splitted peaks in sample a23

(figure 17) should show the distribution of  $\text{Fe}^{2+}$  and  $\text{Mg}^{2+}$  over the B and the C site. Regarding to the site occupancy, electron microprobe cannot give any information. Due to microprobe analysis and the following calculation scheme all  $\text{Fe}^{2+}$  should occupy the B site and C site should be filled completely by  $\text{Mg}^{2+}$ . Based on three appearing peaks, this cannot be true. Sample a23 shows splitting in parallel polarized orientation of two/ three peaks. It is the same effect on different chemical M1M1M3 species. To describe the procedure to calculate the B site, the  $\text{MgMgMg-OH-}\square$  peak is used as an example. In tremolite this peak is found around  $3673 \text{ cm}^{-1}$ . In sample a23 this peaks is splitted and appears at  $3669.6 \text{ cm}^{-1}$  and  $3665.9 \text{ cm}^{-1}$ . By comparison with other samples (e.g. grunerite a16, a9) the lower peak has been identified as  ${}^{\text{B}}\text{Fe-MgMgMg-OH-}\square$  peak and the higher to  ${}^{\text{B}}\text{Mg-MgMgMg-OH-}\square$ . The peak (like the other in this sample) is composed of 65% lower peak and 35% higher peak. Assuming that this effect is due to chemical variation on the B site, this gives 1.3 apfu  ${}^{\text{B}}\text{Fe}^{2+}$  and 0.7 apfu  ${}^{\text{B}}\text{Mg}^{2+}$  on the B site. With this new distribution the  $\text{Mg}^*_\text{C}$  have been recalculated again. Now the  $\text{Mg}^*$

Table 4: Calculation of B-site occupancy based on the splitting of Raman OH-stretching peaks.

Sample	content by splitting	content by emp
a18	0.29 ${}^{\text{B}}\text{Fe}^{2+}$	0.21 ${}^{\text{B}}\text{Fe}^{2+}$
a10	0.35 ${}^{\text{B}}\text{Mg}$	0.12 ${}^{\text{B}}\text{Mg}$
a4	0.27 ${}^{\text{B}}\text{Fe}^{2+}$	0.22 ${}^{\text{B}}\text{Fe}^{2+}$

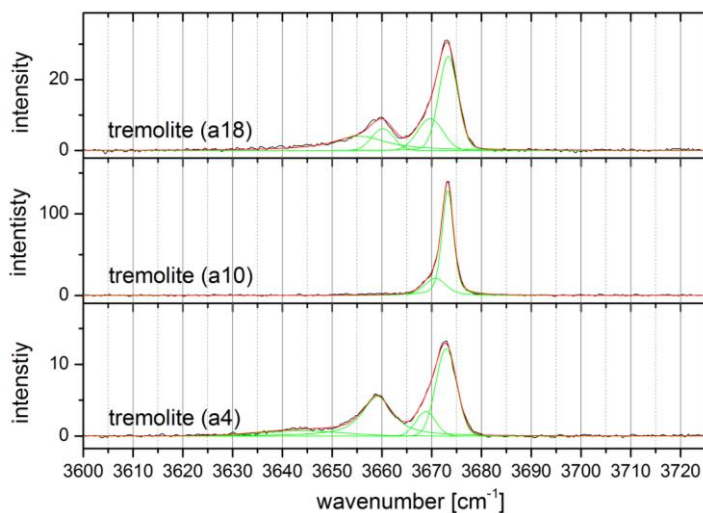


Figure 18: Peak fitting of the asymmetric tremolite samples a18, a10 and a4.

composition of electron microprobe analysis and the Raman- $\text{Mg}^*$  fits even better (figure 15; red). The quantification of the B-site occupancy via the peak splitting however requires good-quality spectra. Therefore this cannot be done for every sample exhibiting subtle peak splitting. Table 4 show some results of samples where the B-site calculation on the basis of the splitting of peaks (figure 18), like explained above, was tried. In sample a4 (tremolite) electron microprobe gives 0.22 apfu  $\text{Fe}^{2+}$  ions, which have to be on the B site (following the standard procedure to fill the crystallographic site); the Raman peak splitting gives 0.27 apfu  $\text{Fe}^{2+}$  on the B site. However this does not fit for all samples. The splitting of a10 (tremolite) shows a high distribution of 13-23% for one splitted peak of different orientations. Also the average  ${}^{\text{B}}\text{Mg}$  of 0.35 apfu do not fit to electron microprobe analysis measurements with 0.12 apfu  ${}^{\text{B}}\text{Mg}$ . The  $\text{MgMgMg}$ -peak of the sample a18 leads to  ${}^{\text{B}}\text{Fe}^{2+}$  composition of 0.29 apfu. This correlates to electron microprobe results of 0.21 apfu  ${}^{\text{B}}\text{Fe}^{2+}$ . Also a37 show an asymmetric  $\text{MgMgMg-OH-}\square$  peak. The calculation corresponds to the B site composition of Na/Ca, although  $\text{Na}^+\text{-O}$  and  $\text{Ca}^{2+}\text{-O}$  should have the same covalence. Therefore this effect may be also related due to one valent B site cation. In contrast sample a25 (cummingtonite) show a strong splitted  $\text{MgMgMg-OH-}\square$  peak. Calculation of

these due to the above describes scheme would give an  ${}^B\text{Fe}^{2+}$  content of 1.44 apfu, but the sample contain in total only about 0.28 apfu  $\text{Fe}^{2+}$  at all. Here the calculation does not work at all. Most samples with splitted peaks in parallel-polarized orientation do not show this splitting in cross-polarized orientation, because the spectra have lower intensities and higher noise.

While samples with  ${}^B\text{Fe}^{2+}$  and  ${}^B\text{Mg}^{2+}$  show clear splitting (two-mode behaviour due to large differences in the degree of covalency in the cation-oxygen interactions), samples with  ${}^B\text{Na}^+$  and  ${}^B\text{Ca}^{2+}$  shows more continuous change in wavenumber (maybe one-mode). Samples containing  ${}^B\text{Ca}^{2+}$  show peaks with higher wavenumber than samples with  ${}^B\text{Na}^+$  or samples with Mg/Fe on the B-site. Because of the change in the charge of the B-site cation, these samples contain a (partially) filled A site or – as

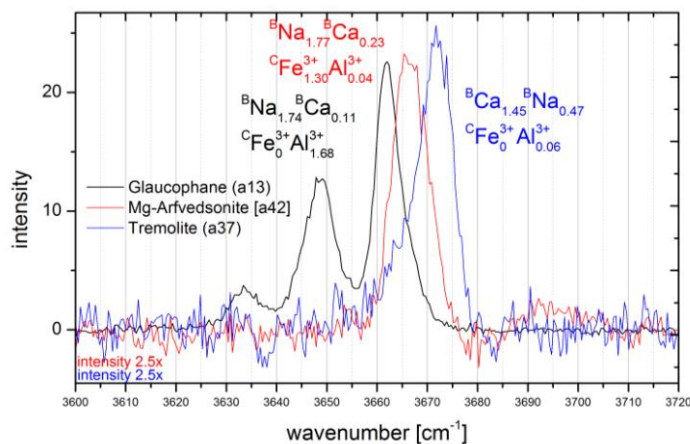


Figure 19: Raman scattering caused by OH-stretching modes for glaucophane (a13), magnesio-arfvedsonite(a42) and tremolite (a37). These samples show continuous change in wavenumber due to the change in the B-site and C(M2)-site composition.

the samples in figure 19 - trivalent cations on the C site. The high charge cations (like  $\text{Fe}^{3+}$  and  $\text{Al}^{3+}$ ) occupy presumably the M2 site (Oberti et al., 2007). Therefore the effect of  ${}^B\text{Na}^+$  cannot consider separately and there may be an additional effect of M2 site. Due to the same covalence of the bonding of  $\text{Ca}^{2+}\text{-O}$  and  $\text{Na}^+\text{-O}$  there should be no change in peak position. In figure 19 a change of peak position is obviously. Therefore this may be an effect of M2 site, which is indirectly influenced by one valent B-site cations, because of electron neutrality. Figure 19 shows that the OH bond stretching mode of glaucophane with  $\text{Al}^{3+}$  at M2 site show lower wavenumbers than the same MgMgMg-OH-□ peak in Mg-arfvedsonite sample which have similar B site composition but  $\text{Fe}^{3+}$  at M2 site. This could be a hint, that  $\text{Fe}^{3+}$  at M2 site shifts the peak to lower wavenumbers than  $\text{Al}^{3+}$  at M2 site.

Samples a13 (glaucophane) and a28 (clino-ferro-holmquistite) show similar  $\text{Al}^{3+}$  content on C-site, as well as comparable A-site and W-site composition. The  $\text{Mg}^{2+}$ - and  $\text{Fe}^{2+}$ -content is different, which can be seen by the intensity distribution of the appearing peaks. The small shift of the peak position can be therefore attributed to variations in the B-site composition (figure 20). Clino-fero-holmquistite contains  ${}^{\text{B}}\text{Li}^+$  while glaucophane contain  ${}^{\text{B}}\text{Na}^+$ . One can assume that the OH bond stretching of  ${}^{\text{C}}\text{Fe}{}^{\text{C}}\text{Mg}{}^{\text{C}}\text{Mg}\text{-OH-}{}^{\text{A}}\square$  with adjacent  ${}^{\text{B}}\text{Na}^+$  appears at  $3648\text{ cm}^{-1}$ ,

whereas that of  ${}^{\text{C}}\text{Fe}{}^{\text{C}}\text{Mg}{}^{\text{C}}\text{Mg}\text{-OH-}{}^{\text{A}}\square$  with adjacent  ${}^{\text{B}}\text{Li}^+$  is at  $3646\text{ cm}^{-1}$ . However the change in the wavenumber approaches the spectral resolution. Therefore this shift has to be considered with care.

Experimental evidences of Welch & Knight (1999) showed that the  ${}^{\text{C}}\text{Al}^{3+}$  can be dispersed over M2 and M3, indicated by shorter M3-O than M1-O bond length. But in glaucophane (and fluoro-amphiboles) they prefer to occupy the M2 site (Oberti et al., 2007).  ${}^{\text{C}}\text{Al}^{3+}$ -containing samples show better results regarding the agreement between  $\text{Mg}^*$  determines from electron microprobe analysis and Raman spectroscopy when the  $\text{Mg}_{\text{Li}}^*$  ratio is used. The  $\text{Mg}_{\text{Al}}^*$  ratio, which includes the  ${}^{\text{C}}\text{Al}^{3+}$  content, shows huge deviation from the  $\text{Mg}_{\text{Raman}}^*$  ratio. This could be a hint that the high-charge ion of  $\text{Al}^{3+}$  prefers to occupy the M2-site, which in general should not influence the Raman spectra as much as the M3 and M1 site.

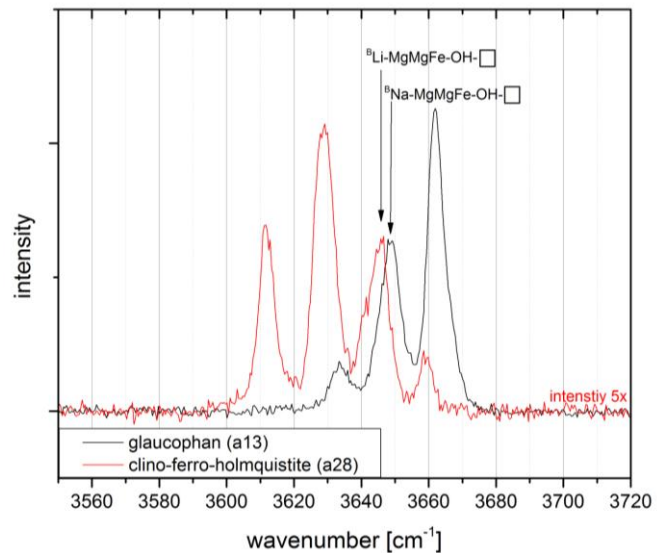


Figure 20: Raman scattering of  ${}^{\text{C}}\text{Al}^{3+}$  containing samples glaucophane (a13) and clino-ferro-holmquistite (a28) generated by OH-stretching modes. The small peak shift is due to variations in the B-site composition.



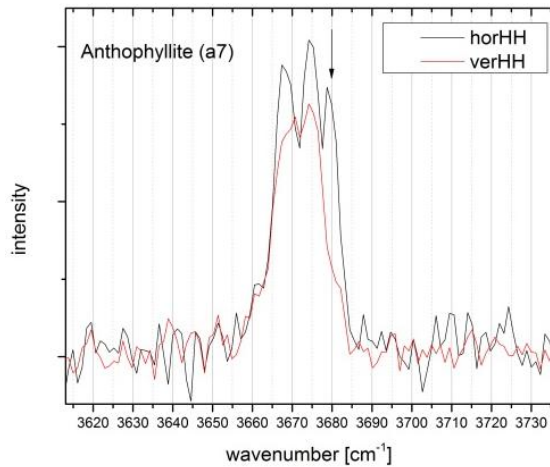


Figure 21: The OH-stretching mode of anthophyllite (a7) shows splitting in 3 peaks. The intensity of the highest wavenumber component (marked by the arrow) exhibits strong orientation-dependence.

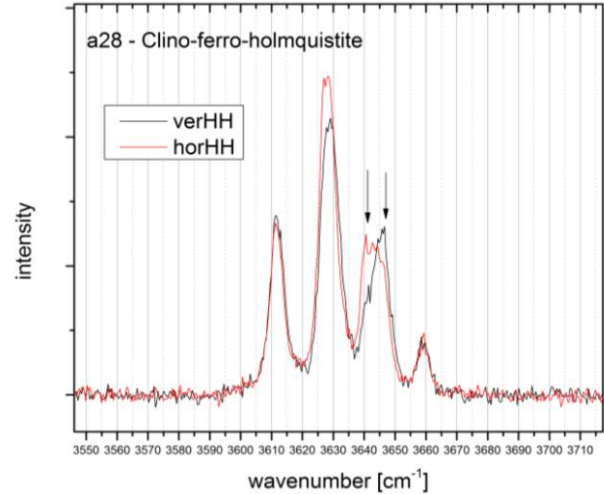


Figure 22: Sample a28 (clino-ferro-holmquistite) shows one orientation dependent peak, which changes in asymmetric shape from horizontal to vertical orientation.

Some samples show orientation dependence of the peak splitting. For example a7 (anthophyllite) shows different number of split components in horHH and verHH configurations (figure 21). The intensity of the highest-wavenumber Raman signal at ca.  $3679 \text{ cm}^{-1}$  shows strong orientation dependence and it appears as a well-resolved peak in the vertical spectra but in the horizontal spectra it appears only as a shoulder. Furthermore a28 (clino-ferro-holmquistite) shows one asymmetrically shaped peak, whose maximum is positioned at  $3540.8 \text{ cm}^{-1}$  and  $3646.1 \text{ cm}^{-1}$  in horizontal and vertical orientation, respectively (figure 22). One can speculate that this bond is two-component and the intensity ratio between the two components depends on the orientation of the crystallographic axis with respect to the polarization of the incident light. X-ray diffraction analysis (XRD) indicates that a7 is orthorhombic. Also a28 may occur in orthorhombic structure. Therefore this orientation dependence of OH stretching modes might be a hint on orthorhombic structure. However the micrometer-scale chemical inhomogeneity cannot be eliminated as a reason. Due to the change of the orientation of the sample another point might have been measured.

All Raman peaks attributed to the filled A site are broader. In figure 23 this trend is marked by two red lines. Against the sample-choosing-criteria, some samples turned out to contain  $\text{Al}^{3+}$  on the T-site. Most of these samples show larger full width at half maximum (FWHM). One  $\text{TAl}^{3+}$ -free sample (grey) however also show considerably large FWHM. This is a  $\text{C}^{\text{Li}^+}$  containing sample (a36) (the Raman spectra of the OH stretching modes can be seen in

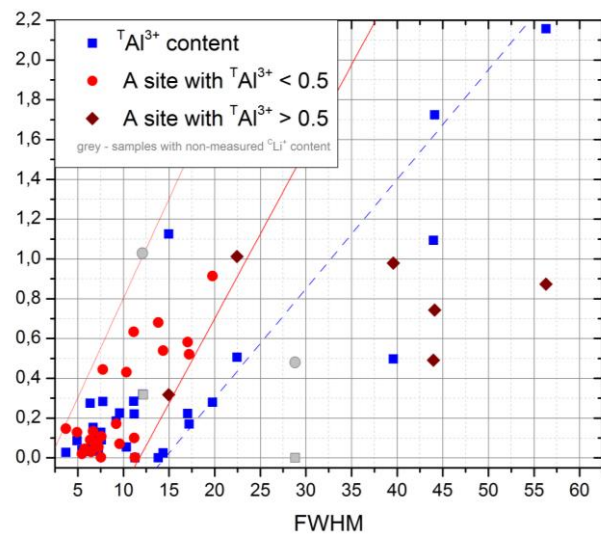


Figure 23: A site occupation and  $\text{TAl}^{3+}$  content versus the full width at half maximum (FWHM) of OH bond stretching mode.

figure 28). However, if higher  $\text{Li}_2\text{O}$  amount for this sample is assumed, the A site occupancy changes to a completely filled A site (table 5). Therefore the Li-containing samples have to be handled with care until the Li-content have been measured by additional methods.

Table 5: Change in  $\text{Li}^+$  assumption (marked in red) for sample a36 changes also the occupancy of A site (marked in green). Without additional measurements of  $\text{Li}^+$  these calculations have to be handled with care.

assuming high Li amount	$(\text{Na}_{0,62}\text{K}_{0,42})^{\text{A}}(\text{Na}_{0,84}\text{Mn}_{0,47}\text{Li}_{0,69})^{\text{B}}(\text{Li}^+_{1,02}\text{Fe}^{3+}_{1,14}\text{Mg}_{2,19}\text{Fe}^{2+}_{0,48}\text{Al}_{0,11}\text{Ti}_{0,06})^{\text{C}}\text{Si}_8^{\text{T}}\text{O}_{22}(\text{OH}_{1,11}\text{F}_{0,74}\text{O}^{2-}_{0,12})$
assuming low Li amount	$(\text{Na}_{0,06}\text{K}_{0,42})^{\text{A}}(\text{Na}_{1,39}\text{Mn}_{0,47}\text{Li}_{0,14})^{\text{B}}(\text{Li}^+_{1,02}\text{Fe}^{3+}_{1,56}\text{Mg}_{2,19}\text{Al}_{0,11}\text{Ti}_{0,06})^{\text{C}}\text{Si}_8^{\text{T}}\text{O}_{22}(\text{OH}_{1,13}\text{F}_{0,74}\text{O}^{2-}_{0,12})$

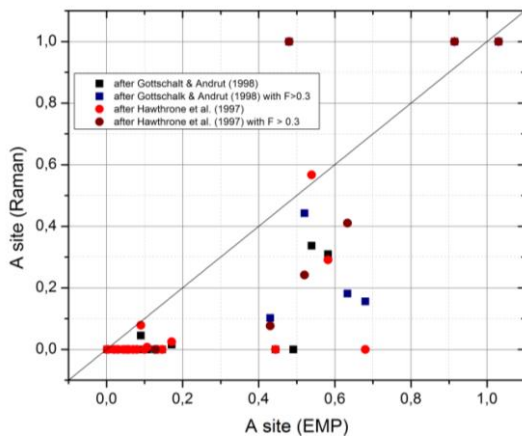


Figure 24: Tried A site calculations do not show usable results.

The broadening of these peaks may also be caused by overlapping of several peaks, like  $\text{MgMgMg-OH-}^{\text{A}}\text{Na-OH}$ ,  $\text{MgMgMg-OH-}^{\text{A}}\text{K-OH}$ ,  $\text{MgMgFe-OH-}^{\text{A}}\text{Na-OH}$  and  $\text{MgMgFe-OH-}^{\text{A}}\text{K-OH}$ , because the shift of  $^{\text{A}}\text{Na}$  and  $^{\text{A}}\text{K}$  is similar but slightly different. Nearly all samples with  $\text{Na}^+$  on the A-site also contain  $\text{K}^+$  or  $\text{Ca}^{2+}$  on the A-site. Therefore instead of e.g. two peaks there are four overlapping peaks with only small shift difference. Two calculations of filling of the A site based on the Raman data have been tried (figure 24). First a calculation following the Mg-Fe calculation procedure comparable to that mentioned in Gottschalk & Andrut (1998) has been performed. Therefore the ratio between M1M1M3-OH-A-OH peaks to all peaks has been calculated. A second A-site calculation was done following Hawthorne et al. (1997). Here also a change of the factor  $k$  has been tried. Both calculations do not show usable results. For low degree of A-site occupancy this may be due to the background in combination with the broad A-site bands so that they are not resolvable. For high degree of A site occupancy the calculated Raman A site is always to low, which may be due to fluorine at the W-site, which maybe prefer W site where A site is filled. The IR spectroscopy studies have used synthetic amphiboles without any fluorine content.

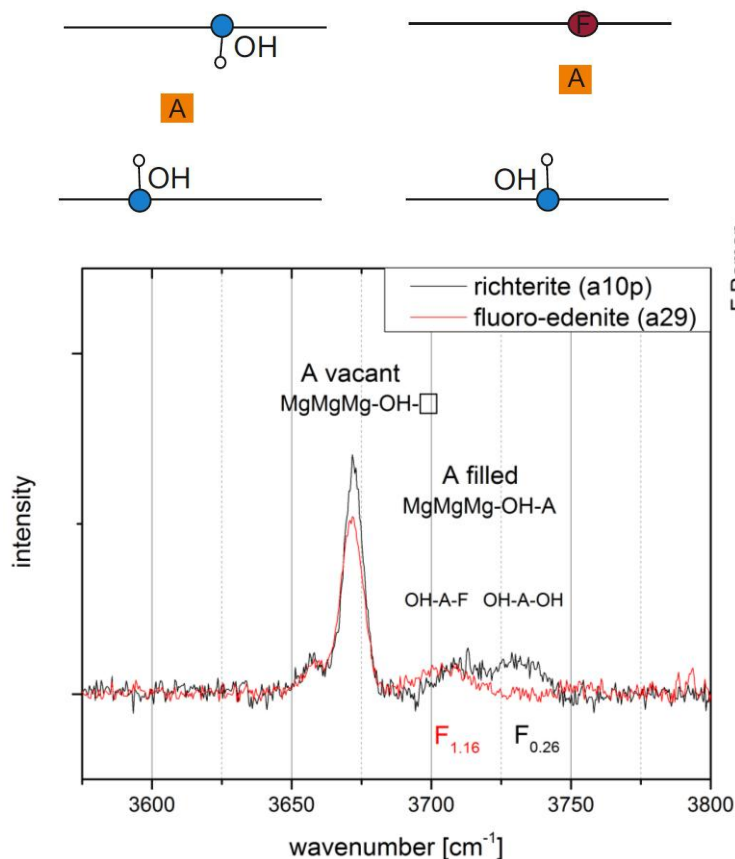


Figure 25: **Top:** Schematic presentation of the effect of fluorine with filled A site (after Robert et al. (1999)). **Bottom:** OH-stretching spectra of richterite and fluoro-edenite. Both samples have similar chemical composition. The major difference is the fluorine content.

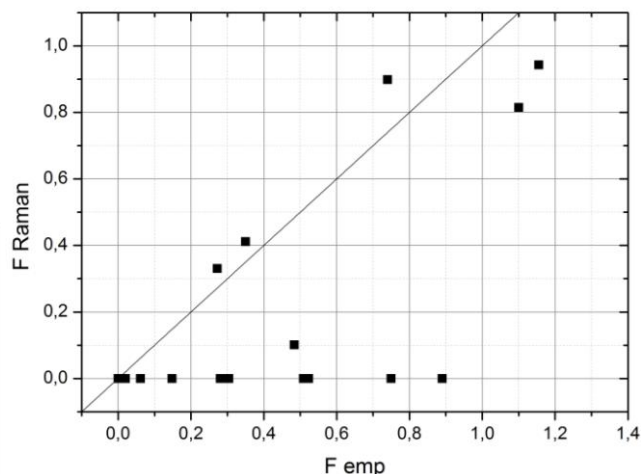


Figure 26: Calculation of fluorine content following the procedure proposed by Robert et al. (1999).

The OH-A-F configuration (see figure 25, top) may also be a reason for broad peaks. Robert et al. (1999) regarded a new infrared OH band at frequencies about 3711 cm<sup>-1</sup> or 3714 cm<sup>-1</sup>, which is caused by the presence of fluorine. The A-site cation slightly shifts to the fluorine due to electrostatic forces (figure 25, top). As a result, the strength of OH bond weakens. This effect only appears

if fluorine on the W site, a filled A-site and OH group at the opposite W site are available. The effect of F can be seen also in sample a29 (figure 25). The MgMgMg-OH-□ peak is the strongest peak, found at 3671.5 cm<sup>-1</sup>. The OH stretching mode corresponding to filled A site (A-filled mode) should show a shift about 50-60 cm<sup>-1</sup> towards higher wavenumber. However the peak appears at 3704 cm<sup>-1</sup>. This indicates a high amount of MgMgMg-OH-A-F configuration compared to MgMgMg-OH-A-OH configuration. The electron microprobe confirms this with a high fluorine content of 1.15 apfu. Figure 25 (at the bottom) compares sample a10p (richterite, with half-filled A-site) and a29 (fluoro-edenite 60% filled A-site). While a29 contains >1 apfu F<sup>-</sup>, a10p contain only 0.27 apfu F<sup>-</sup>. The chemical composition of these samples is comparable. As a result of the higher F<sup>-</sup>-content in a29 there is only one peak arising from OH adjacent to filled A site, while a10p, shows two such modes. Also the A-vacant mode of a29 shows a decrease in intensity. Robert et al (1999) also presented a calculation of fluorine content on the basis of the new band. For all samples with an amount of filled A-site > 0.4 this calculation was tried. The results can be seen in figure 26. For most samples the Raman results do not match with the electron microprobe analysis data. Only five samples (a10p, a29, a33, a36 and a39) show comparable fluorine contents. The discrepancy for the rest may result from strong micrometer-scale chemical inhomogeneity of F and the unavoidable mismatch of spatial points measured by Raman spectroscopy and EMP. Nevertheless, the results point out that this calculation

based on Raman data is not sufficiently reliable to estimate the fluorine content in amphiboles. In samples with high F content the configuration M1M1M3-F-A-F (and M1M1M3-F-□-F) should appear and cannot be seen in Raman spectra. Also the peak related to MgMgMg-OH-A-F may overlap with peaks related to MgFeFe-OH-A-OH.

Sample a34 and a35 (figure 27) do not contain Mg, but fluorine and a filled A site. The expected peak, due to the above described concept of FeFeFe-OH-A composition, should be in the range of  $3675\text{ cm}^{-1}$  to  $3720\text{ cm}^{-1}$ . However, the bands appear in the range of  $3637$  to  $3679\text{ cm}^{-1}$ . This is due to the effect of fluorine, which leads to a decrease in the wavenumber. In figure 15 these samples can be seen in blue at the left site, with a high discrepancy between electron microprobe and Raman spectroscopy. Because the peaks appear in the range of  $3637$  to  $3679\text{ cm}^{-1}$  which is for the calculation scheme of all samples, defined as MgMgFe-OH-□ peaks, they have been misinterpreted as such peaks and the Raman

calculation have been wrong. Only the broadening of the peaks may be an indicator for A-site occupancy, but without electron microprobe analysis the Raman peaks cannot be distinguished correctly. To verify broad peaks arising from filled A site and arising from  ${}^T\text{Al}^{3+}$  further studies have to be done.

As expected, sample with high amount of  $\text{O}^{2-}$  and low OH<sup>-</sup> at W site (a40, ferri-kaersutite), do not show any OH stretching modes.

Raman spectroscopy would be an advantage over electron microprobe if it is possible to determine the  $\text{Li}^+$ -content of the amphiboles. Therefore in this study there are two samples with  ${}^B\text{Li}^+$  and three samples with possible  ${}^C\text{Li}^+$ . The determination of  ${}^B\text{Li}^+$  is challenging, although there is a small shift of  $2\text{ cm}^{-1}$  to lower frequencies between glaucophane (a13) and clino-ferroholmquistite (a28) shown in figure 20. However since there are only few samples with  ${}^C\text{Al}^{3+}$  and both  ${}^B\text{Li}^+$  samples contain  ${}^C\text{Al}^{3+}$  a certain determination of  ${}^B\text{Li}^+$  and  ${}^C\text{Al}^{3+}$  cannot be done. Determination of  ${}^C\text{Li}^+$  should

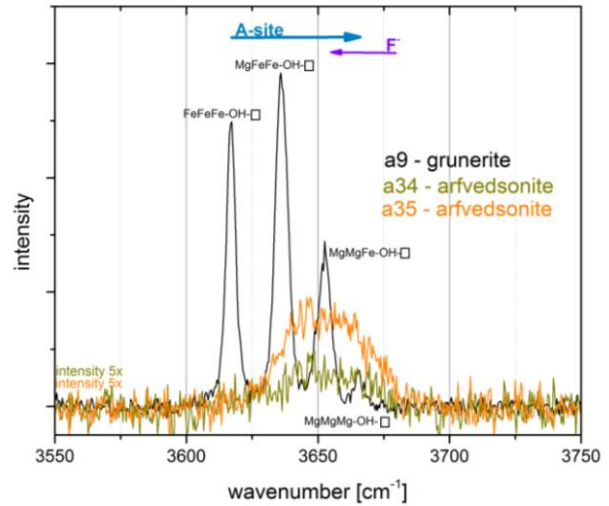


Figure 27: Filled A site (effect marked by the blue arrow),  $\text{Al}^{3+}$  on the T site and F on the W site (effect marked by the violet arrow) of samples a34 and a35 caused wrong peak assignment to M1M1M3 species.

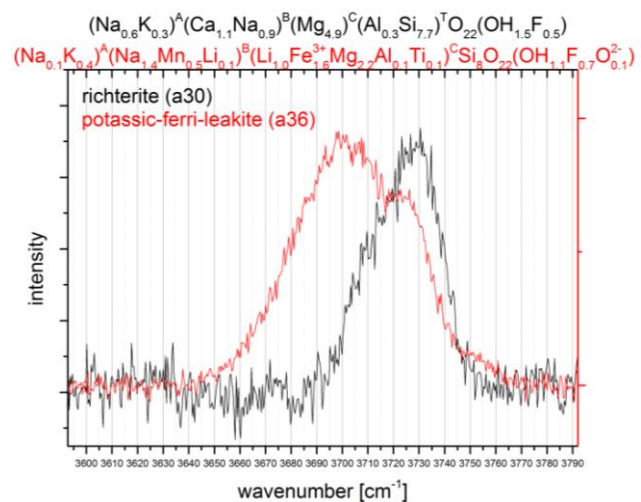


Figure 28: Raman scattering resulting from OH-stretching modes of richterite (a30) and  ${}^C\text{Li}$  containing potassic-ferri-leakite (a36). The negative peak shift of  $-30\text{ cm}^{-1}$  may be due to  ${}^C\text{Li}$ .

be possible because  ${}^{\text{C}}\text{Li}^+$  occupies the M3 site, observed by low site scattering of M3 (Oberti et al., 2007). But the determination of  ${}^{\text{C}}\text{Li}^+$  is also problematic, because all three samples show broad peaks, where no clear differentiation of the peaks can be done. Comparing sample a30 (richterite) with a36 (potassic-ferri-leakite) a shift of ca  $30\text{ cm}^{-1}$  to lower frequencies can be seen (figure 28). This could be due to the  ${}^{\text{C}}\text{Li}^+$  content, but also the effect of  ${}^{\text{C}}\text{Fe}^{3+}$  is unknown and can play a role here, as well as the presence of  ${}^{\text{C}}\text{Fe}^{2+}$  cannot be eliminated (because the  $\text{Fe}^{2+}/\text{Fe}^{3+}$  content was recalculated and not measured). Also the different composition of B-site of the samples should have an effect. Synthetic samples with better defined chemistry should be studied to clarify this issue.

### 3.3. Sources of errors

The basic errors of Raman spectroscopy are diverse. The spectral resolution is about  $\sim 2 \text{ cm}^{-1}$  with a visible laser and  $3 \text{ cm}^{-1}$  with a UV laser. For reliable results the different shifts have to be larger than the spectral resolution. As already described above, the change of the laser can produce shifts of about  $3 \text{ cm}^{-1}$ . Because of (sometimes very high) photoluminescence a background correction has to be done manually. Therefore human failure can also leads to uncertainties in the peak intensities in samples with strong photoluminescence background. A huge problem of Raman spectroscopy at natural samples is the background. Especially amphiboles have sometimes strong photoluminescence and a rough surface. The rough surface can be eliminated with polishing the sample, which would need preparation. With strong photoluminescence another point of the sample or another laser wavelength should be used. The photoluminescence is particularly a problem to study the OH-stretching modes, because the

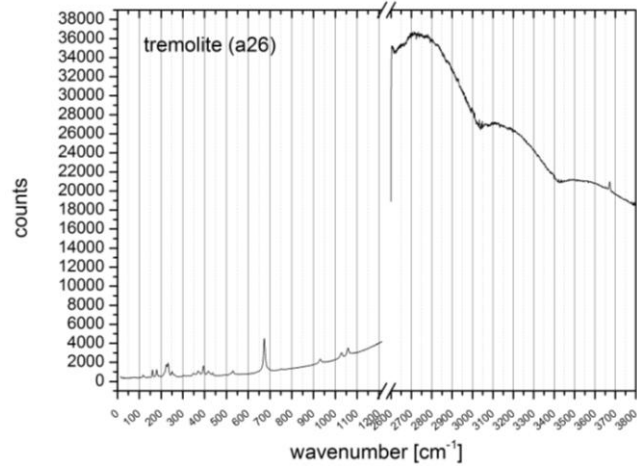


Figure 29: Sample a26 shows strong continuum background due to fluorescence. The analysis of the Raman peaks could only be done after the baseline correction.

photoluminescence peak often appears in the same range as continuous background. The lower-wavelength spectra ( $15\text{-}1215 \text{ cm}^{-1}$ ) often are not influenced so much. Figure 29 shows

the uncorrected spectra of a26 (tremolite), which exhibited the highest background among all samples.

As described above for sample a34 and a35 (figure 27), wrong assignment of peaks can lead to wrong results, if only the peak position is considered to determine the peak. Sometimes, especially in samples with a filled A site, a detailed determination cannot be done due to broad peaks and the effect of fluorine only can be estimated.

The measurement errors of electron microprobe are very small. But due to the lack of determining  $\text{Li}^+$ ,  $\text{H}^+$  and valence of iron, errors can arise while calculating the chemical formula. The error in  $\text{Li}^+$ ,  $\text{OH}^-$  and  $\text{Fe}^{3+}$  therefore cannot be eliminated without additional measurements.

The errors of the  $\text{Mg}^*$  ratio based on Raman data is calculated with the errors of the normalized intensities of the fittings:

$$\text{errMg}^* = \frac{(3I_{\text{MMM}} + 2I_{\text{MMF}} + I_{\text{MFF}}) * (3eI_{\text{MMM}} + 2eI_{\text{MMF}} + eI_{\text{MFF}}) + (3I_{\text{MMM}} + 3I_{\text{MMF}} + 3I_{\text{MFF}} + 3I_{\text{FFF}}) * (3eI_{\text{MMM}} + 3eI_{\text{MMF}} + 3eI_{\text{MFF}} + 3eI_{\text{FFF}})}{(3I_{\text{MMM}} + 3I_{\text{MMF}} + 3I_{\text{MFF}} + 3I_{\text{FFF}})^2}$$

where  $I$  is the normalized intensity (of  $\text{MMM}=\text{MgMgMg-OH}$  peak,  $\text{MMF}=\text{MgMgFe-OH}$  peak,  $\text{MFF}=\text{MgFeFe-OH}$  peak,  $\text{FFF}=\text{FeFeFe-OH}$  peak) and  $eI$  is the error on the normalized intensities due to the fit. Therefore the total error depends on the goodness of the fittings.

### 3.4. Comparison to infrared spectroscopic studies

By comparing our Raman results with infrared studies by others, a good analogy can be found. The spectra are quite similar and also the OH peaks appear in the same spectral range. The slight frequency difference of 2 - 3  $\text{cm}^{-1}$  mentioned in Apopei & Buzgar (2010), can be confirmed in this study. A comparison between the positions of infrared and Raman peaks is given in table 6.

The above mentioned splitting of peaks also appears in infrared spectra. Some authors interpret this as sole influence of the B-site composition (Chen et al. (2004), Hawthorne et al. (1997), Gottschalk & Andrut (1998)), others consider this as a combined effect of M2-site and the B-site composition (Hawthorne & Della Ventura (2007), Iezzi et al. (2005)), whereas some authors have suggested that this results from different Mg/Fe-configuration distributed over M(1)- and M(3)-site (Wang et al., 1988) or from difference between O3A-H1 and O3B-H2 (Ishida & Hawthorne, 2003). This Raman spectroscopic study shows that the splitting seems to be caused predominantly by the B-site composition. However an influence of M2-site chemistry cannot be completely eliminated. More complex clustering of  $\text{Mg}^{2+}$  and  $\text{Fe}^{2+}$  over M1 and M3 as the splitting effect can be eliminated because the  $\text{MgMgMg-OH-}\square$  peak also shows splitting.

Robert et al. (1999) reported a new band due to fluorine on the W site. This fluorine-induced OH band can also be seen in the Raman spectra. In their study they presented a good fit of the calculation of fluorine-content due to the 3711  $\text{cm}^{-1}$  band. In this study an attempt has also been made to calculate the F-content on the basis of the fluorine-induced band at 3711  $\text{cm}^{-1}$ . This calculation did not give reliable results and therefore it is not applicable on Raman spectra or/and the used natural samples (figure 26).

The calculation of A-site occupancy by IR spectroscopy mentioned in Hawthorne et al. (1997) and Iezzi et al. (2004) does not fit for the Raman spectroscopic results at all. Even a changed factor  $k$  does not show consistent results. Also the calculations of A-site occupancy, following the IR spectroscopic calculations of Gottschalk & Andrut (1998) by Raman spectra did not get the desired results (figure 24). Quantitative statements about the A-site occupancy therefore cannot be done by Raman spectroscopy at natural samples.

Table 6: Comparison of the position of infrared (left) and Raman (right) peaks originating from OH-stretching modes. Data in good agreement are marked in blue.

Waveno.	A	M4	M1	M1	M3	M2	W	Reference	Waveno.	A	M4	M1M1M3	M2	W	Sample		
3614		Li	Fe <sup>2+</sup>	Fe <sup>2+</sup>	Fe <sup>2+</sup>	Fe <sup>3+</sup>	OH	lezzi et al. (2005, 2004), Kloprogge 2001	3611		Li	Fe <sup>2+</sup>	Fe <sup>2+</sup>	Fe <sup>2+</sup>	Al/Mg/ Fe <sup>3+</sup>	OH	a28
3618			2Fe <sup>2+</sup> +Al				OH	Law & Whittaker (1981)	3717		Fe <sup>2+</sup>	Fe <sup>2+</sup>	Fe <sup>2+</sup>	Fe <sup>2+</sup>	Mg/ Fe <sup>2+</sup>	OH	a9
									3718		Fe/Mn	Fe	Fe	Fe	Mg/ Fe <sup>2+</sup>	OH	a16, a17
3626		Ca	Fe <sup>2+</sup>	Fe <sup>2+</sup>	Fe <sup>2+</sup>		OH	Chen et al (2004)									
3631		Li	Mg	Fe <sup>2+</sup>	Fe <sup>2+</sup>	Fe <sup>3+</sup>	OH	lezzi et al. (2005, 2004), Kloprogge (2001)	3629/3630		Li	Mg	Fe <sup>2+</sup>	Fe <sup>2+</sup>	Al/Mg	OH	a27
3634		Na	Mg+2Fe <sup>2+</sup>				OH	Su et al. (2009), Kloprogge (2001)	3633		Na	Mg	Fe <sup>2+</sup>	Fe <sup>2+</sup>	Al/Mg	OH	a13
3634			Mg+ Fe <sup>2+</sup> +Al				OH	Law & Whittaker (1981)	3635		Fe <sup>2+</sup>	Mg	Fe <sup>2+</sup>	Fe <sup>2+</sup>	Mg/ Fe <sup>2+</sup>	OH	a23, a9
									3637		Fe/Mn	Mg	Fe <sup>2+</sup>	Fe <sup>2+</sup>	Mg/ Fe <sup>2+</sup>	OH	a17, a16
									3639		Mg	Mg	Fe <sup>2+</sup>	Fe <sup>2+</sup>	Mg/ Fe <sup>2+</sup>	OH	a23
3645		Ca	Mg	Fe <sup>2+</sup>	Fe <sup>2+</sup>		OH	Chen et al. (2004)	3644		Ca	Mg	Fe <sup>2+</sup>	Fe <sup>2+</sup>	Mg/ Fe <sup>2+</sup>	OH	a19
3647		Li	Mg	Mg	Fe <sup>2+</sup>	Fe <sup>3+</sup>	OH	lezzi et al. (2005, 2004), Kloprogge (2001)	3646		Li	Mg	Mg	Fe <sup>2+</sup>	Al/Mg	OH	a27
3646-3649		Na	Mg	Mg	Fe <sup>2+</sup>			Su et al. (2009)	3648		Na	Mg	Mg	Fe <sup>2+</sup>	Al/Mg	OH	a13
3651			2Mg+Al				OH	Law & Whittaker (1981)	3651/3652		Fe	Mg	Mg	Fe <sup>2+</sup>	Mg/ Fe <sup>2+</sup>	OH	a23,a9
									3653		Fe/Mn	Mg	Mg	Fe <sup>2+</sup>	Mg/ Fe <sup>2+</sup>	OH	a17, a16
3658-3660		Na	Mg	Mg	Mg			Su et al. (2009)	3655		Mg	Mg	Mg	Fe <sup>2+</sup>	Mg/ Fe <sup>2+</sup>	OH	a23
3661		Ca	Mg	Mg	Fe <sup>2+</sup>		OH	Chen et al. (2004)	3659		Ca	Mg	Mg	Fe <sup>2+</sup>	Mg/ Fe <sup>2+</sup>	OH	a19, a18, a4
3662		Li	Mg	Mg	Mg	Fe <sup>3+</sup>	OH	lezzi et al. (2005, 2004), Kloprogge (2001)	3659/3660		Li	Mg	Mg	Mg	Al/Mg	OH	a27
									3661		Na	Mg	Mg	Mg	Al/Mg	OH	a13
									3664		Na	Mg	Mg	Mg	Mg/Fe <sup>2+</sup>	OH	a37
									3666		Na/Ca	Mg	Mg	Mg	Mg/ Fe <sup>3+</sup>	OH	a42
3668		Mg,Fe <sup>2+</sup>	Mg	Mg	Mg		OH	lezzi (2004)	3666/3668		Fe	Mg	Mg	Mg	Mg/ Fe <sup>2+</sup>	OH	a23, a18



3670		Mg	Mg	Mg	Mg	Mg	OH	Hawthorne et al. (1997)	3669/3670		Mg	Mg	Mg	Mg	Mg	OH	a23
3674.2		Mg	Mg	Mg	Mg			Chen et al. (2004)									
3675		Ca	Mg	Mg	Mg		OH	lezzi (2004), Chen et al. (2004)	3672/3673		Ca	Mg	Mg	Mg	Mg	OH	a4, a5, a10, a18, a19, a21, a29, a37, a24, a26, a41
3678	Na	Ca	Mg	Mg	Al		OH	Oberti et al. (2007)									
3676.9		Ca	Mg	Mg	Mg			Chen et al. (2004)									
3693	Li		Mg	Mg	Fe <sup>2+</sup>		OH	lezzi (2004)									
3709	Li		Mg	Mg	Mg		OH	lezzi (2004)									
3711	Na	Ca	Mg	Mg	Mg	Mg	F, OH	Robert et al. (1999)	ca. 3707	Na/K	Ca/Na	Mg	Mg	Mg	Mg/ Fe <sup>2+</sup>	OH/F	a10p, a25
3714	K	Ca	Mg	Mg	Mg	Mg	F, OH	Robert et al. (1999)									
3730	Na	Ca	Mg	Mg	Mg	Mg	OH	Robert et al. (1999)	ca. 3730	Na/K	Ca/Na	Mg	Mg	Mg	Mg/ Fe <sup>2+</sup>	OH	a10p
3734	K	Ca	Mg	Mg	Mg	Ca	OH	Hawthorne et al. (1997), Hawthorne & Della Ventura (2007)									

## 4. Conclusion

### 4.1. Application

The application of Raman spectroscopy to study crystallo-chemical composition of amphiboles on

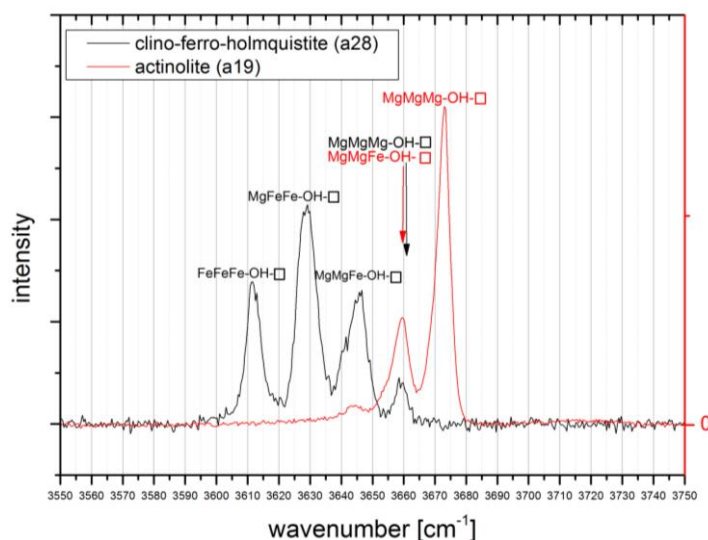


Figure 30: Comparison of ferro-holmquistite (a28) and actinolite (a19). The position of the MgMgMg-OH-□-peak of a28 is close to the position of the MgMgFe-OH-□-peak of a19. This complicates the determination of the peaks.

the basis of the OH-stretching mode is as good as infrared spectroscopy. Always the whole Raman spectra should be considered. Even by studying only the OH-range, all peaks should be examined together, because for example the Li-MgMgMg-OH-□ peak and the Ca-MgMgFe-OH-□ peak may appear in the same wavenumber-range. Examining only this peak can produce wrong estimations.

Therefore further comprehensive analysis of the spectral range 15-1215  $\text{cm}^{-1}$  is necessary. Figure 30 demonstrates possible

misinterpretation based only on the OH bond stretching spectral range. Here there is the problem of peak misassignment. To get the right determination of peaks related to vacancy at A site, the highest- and lowest-wavenumber peak should be considered. Then one of these peaks should be assigned to MgMgMg or FeFeFe, depending on the wavenumber. The other two intermediate peaks can be determined by following the appearance with MgMgFe and MgFeFe. The case that neither the MgMgMg nor the FeFeFe-peak appears in an amphibole with vacant A site is unlikely, because of statistic distribution. If the sample contains filled A-sites and fluorine on the W site, the determination of peaks is more difficult. This can also lead to wrong peak determinations, as described above for sample a34 and a35 (figure 27), due to broad peaks of the filled A-site and the new appearing band with fluorine.

Some peaks appear asymmetric in shape. This asymmetry can be due to small splitting, comparable to the sample a23 (cummingtonite), shown above (figure 17). This splitting can be a hint for the B-site composition. Based on this splitting the composition of B-site can be analysed. Still these calculations should be handled with care, because most spectra are not good enough for detailed analysis of the B-site. However, even not high-quality-spectra with asymmetric peaks can indicate, that the B-site is composed of two different cations with significant differences, like  $\text{Fe}^{2+}$  and  $\text{Mg}^{2+}$  or  $\text{Ca}^{2+}$ .

The broadening of peaks can result from many reasons: A-site occupancy, overlapping of peaks,  $\text{Al}^{3+}$  on the T site or fluorine content in combination with a filled A site. If broad peaks exist in the spectra, the data have to be handled with care and their interpretation is difficult. Then the assignment of the structural composition to the peaks is problematic and all four above named parameters, which lead to broad peaks, should be considered.

## 4.2 Summary

Raman spectroscopy of the OH stretching modes of amphiboles ( $\text{A}_{0-1}\text{B}_2\text{C}_5\text{T}_8\text{O}_{22}\text{W}_2$ ) is a good method to study the crystallochemical composition. Therefore parallel polarized measurements turned out to achieve the best spectra. The C site composition, namely on the M1M1M3 triplet, of the dominant cations  $\text{Fe}^{2+}$  and  $\text{Mg}^{2+}$  can be determined (by the  $\text{Mg}^*$  ratio) with good agreement to electron microprobe analysis. Only samples with filled A site (with or without F content) and  $^{\text{T}}\text{Al}^{3+}$  can lead to wrong results due to broad bands. The determination of  $^{\text{C}}\text{Al}^{3+}$  and  $^{\text{C}}\text{Fe}^{3+}$  is still problematic, because  $^{\text{C}}\text{Al}^{3+}$  and  $^{\text{C}}\text{Fe}^{3+}$  appear at M2 site and therefore cannot be seen directly with Raman spectroscopy of the OH bond stretching mode.  $^{\text{C}}\text{Li}^+$  is still an open question and for clear verification in this study not enough samples were analyzed. Due to broad peaks at high wavenumbers the occupancy of A site can be estimated, although a detailed calculation is not possible. On the basis of small peak shifts and/or splitting of peaks of high quality Raman spectra, estimations about the B site can be done. Due to the splitting or asymmetry of peaks the composition of  $\text{Fe}^{2+}/\text{Mg}^{2+}/\text{Ca}^{2+}$  at B site can be estimated. The small shifts of peaks towards lower wavenumbers may be a hint on one valence cations at B site. With another band which is related to the configuration  $\text{MgMgMg-OH-A-F}$  an estimation of F-content can be done. This does not always reach good results because different compositions (for example F-A-F or  $\text{MgMgMg-OH-}\square\text{-F}$ ), that can appear but not be seen, hinders a proper calculation. This study also showed that the infrared Spectra and the Raman spectra of the OH bond stretching modes are comparable but the calculations for A site and F content, that were develop with synthetic amphiboles, not always can be used on natural samples. In combination with other methods Raman spectroscopy of the OH-groups of amphiboles is favoured mainly because it is fast, non-destructive, micrometer-scale sensitive method, which can give additional information about the site occupancies, in particular about the distribution of various M1M1M3 chemical species.

## 4.3 Further Work

As mentioned above more samples with  $^{\text{C}}\text{Al}^{3+}$ ,  $^{\text{C}}\text{Fe}^{3+}$  and  $^{\text{C}}\text{Li}^+$ , as well as  $^{\text{B}}\text{Li}^+$  should be measured with Raman spectroscopy (as well as electron microprobe analysis (to verify the chemical composition), laser ablation (to verify Li), mössbauer spectroscopy (to verify  $\text{Fe}^{3+}$ )) to study the effect of  $\text{Li}^+$ ,  $^{\text{C}}\text{Al}^{3+}$  and  $^{\text{C}}\text{Fe}^{3+}$ . Furthermore some samples with  $^{\text{T}}\text{Al}^{3+}$ , like pargasite and hornblende, should be analyzed, because they are the most common amphiboles in most geological environments. In this study only two “common” amphiboles a12 (pargasite) and a41 (Mg-hornblende) have been analysed. Because of the broad peaks, a detailed study with more such samples is necessary. Also sample a25

(cummingonite) shows an interesting spectra due to  ${}^T\text{Al}^{3+}$  which should be considered much more in detail than it was possible in this study. If the effect of  ${}^T\text{Al}^{3+}$  is known, the determination of broad peaks due to the filled A site and broad peaks related to  ${}^T\text{Al}^{3+}$  should be possible.

In the range of lower wavenumbers the lattice vibrations have to be studied more in detail, because they can provide information about the crystal chemistry of all sites. Also an identification of monoclinic and orthorhombic amphiboles should be possible due to the peaks in the range of lower wavenumbers. Furthermore the possible orientation dependence of OH stretching modes which may be due to orthorhombic structure (a7 and a28) should be studied in detail.

Calculations that were developed for synthetic amphiboles (F- content calculation, A site occupancy calculation) are not always usable for natural sample. Here an adjustment of the calculations has to be considered. Therefore more natural samples with various F content and A site occupancy should be studied more in detail with the focus on this calculations.

## References

- Apopei, A. I., Buzgar, N. (2010) The Raman study of amphiboles. *Analele Științifice ale Universității "Al. I. Cuza" Iași, Geologie.*, **LVI (1)**, pp.57-83.
- Burns, R. G., Strens, R. G. J. (1966) Infrared Study of Hydroxyl Bands in Clinoamphiboles. *Science*, **153**, pp. 890-892.
- Chen, T.-H., Calligaro, T., Pagès-Camagna, S., Menu, M. (2004) Investigation of Chinese archaic jade by PIXE and  $\mu$ Raman spectrometry. *Journal of Applied Physics A*, **79**, pp. 177-180.
- Deer, W.A., Howie, R.A., Zussman, J. (1980) An Introduction to the Rock Forming Minerals, 1<sup>st</sup> ed. 12<sup>th</sup> Impression. London: Longman Group Limited.
- Della Ventura, G., Redhammer, G. J., Iezzi, G., Hawthorne, F. C., Papin, A., Robert, J.-L. (2005) A Mössbauer and FTIR study of synthetic amphiboles along the magnesioriebeckite – ferri-clinoholmquistite join. *Physics and Chemistry of Minerals*, **32**, pp. 103-112.
- Ferraro, J. R., Nakamoto, K., Brown, C. W. (2003) Introductory Raman Spectroscopy. 2<sup>nd</sup> ed. Academic Press, San Diego, California.
- Gottschalk, M., Andrut M. (1998) Structural and chemical characterization of synthetic (Na, K)-richterite solid solutions by EMP, HRTEM, XRD and OH-valence vibrational spectroscopy. *Physics and Chemistry of Minerals*, **25**, pp. 101-111.
- Gunter, M. E., Belluso, E., Mottana, A. (2007) Amphiboles: Environmental and Health Concerns. In: Hawthorne, F.C., Oberti, R., Della Ventura, G., Mottana, A. (Eds.), *Amphiboles: Crystal Chemistry, Occurrence and Health Issues*, **67**, pp. 453-516. Reviews in Mineralogy & Geochemistry. Virginia: Mineralogical Society of America.
- Hawthorne, F. C. (1981). Crystal Chemistry of the Amphiboles. In Veblen, D. R. (Ed.), *Amphiboles and other hydrous Pyriboles – Mineralogy*, **9A**, 1-102. Mineralogical Society of America.
- Hawthorne, F. C., Della Ventura, G., Robert, J.-L., Welch, M. D., Raudsepp, M., Jenkins, D. M. (1997) A Rietveld and infrared study of synthetic amphiboles along the potassium-richterite–tremolite join. *American Mineralogist*, **82**, pp. 708-716.
- Hawthorne, F. C., Della Ventura, G.(2007). Short-Range Order in Amphiboles. Hawthorne, F.C., Oberti, R., Della Ventura, G., Mottana, A. (Eds.), *Amphiboles: Crystal Chemistry, Occurrence, and Health Issues*, **67**, pp. 172-222. Reviews in Mineralogy and Geochemistry, Mineralogical Virginia: Mineralogical Society of America.
- Hawthorne, F. C., Oberti, R. (2007). Amphiboles: Crystal Chemistry. In Hawthorne, F.C., Oberti, R., Della Ventura, G., Mottana, A. (Eds.), *Amphiboles: Crystal Chemistry, Occurrence, and Health Issues*, **67**, 1–54. Reviews in Mineralogy and Geochemistry, Mineralogical Virginia: Mineralogical Society of America.
- Hawthorne, F. C., Oberti, R., Harlow, G., E., Maresch, W. V., Martin, R. F., Schumacher, J. C., Welch, M. D. (2012) IMA report, Nomenclature of the amphibole supergroup. *American Mineralogist*, **97**, pp. 2031-2048.
- Holland, T., Blundy, J. (1994) Non-ideal interactions in calcic amphiboles and their bearing on amphiboles-plagioclase thermometry. *Contributions to Mineralogy and Petrology*, **116**, pp.433-447.

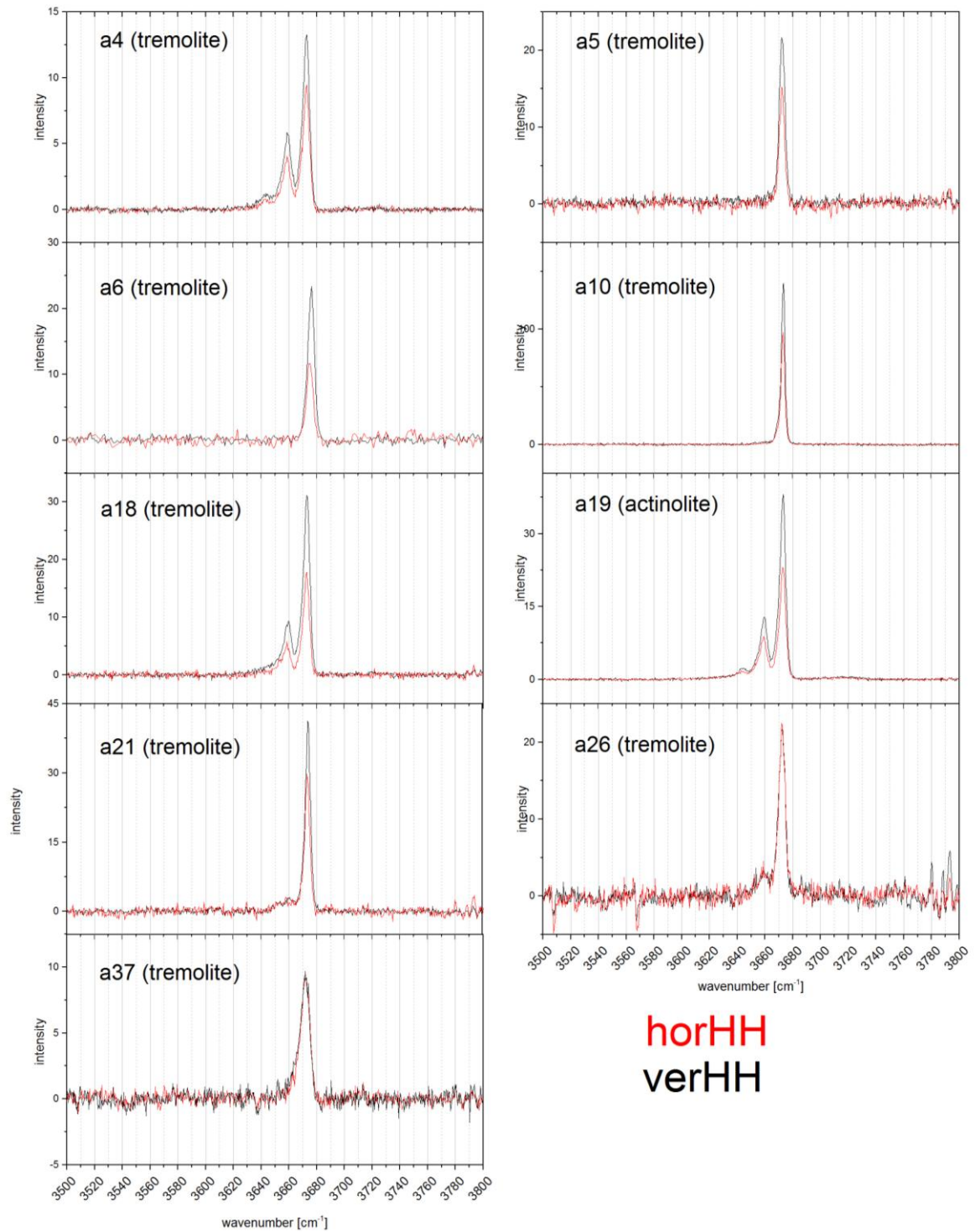
- Iezzi, G., Cámara, F., Della Ventura, G., Oberti, R., Pedrazzi, G., Robert, J.-L. (2004) Synthesis, crystal structure and crystal chemistry of ferri-clinoholmquistite,  $\square\text{Li}_2\text{Mg}_3\text{Fe}^{3+}_2\text{Si}_8\text{O}_{22}(\text{OH})_2$ . *Physics and Chemistry of Minerals*, **31**, pp. 375-385.
- Iezzi, G., Della Ventura, G., Hawthorne, F. C., Pedrazzi, G., Robert, J.-L., Novembre, D. (2005) The  $(\text{Mg},\text{Fe}^{2+})$  substitution in ferri-clinoholmquistite,  $\square\text{Li}_2(\text{Mg},\text{Fe}^{2+})_3\text{Fe}^{3+}_2\text{Si}_8\text{O}_{22}(\text{OH})_2$ . *European Journal of Mineralogy*, **17**, pp. 733-740.
- Iezzi, G., Della Ventura, G., Bellatreccia, F., Lo Mastro, S., Bandli, B. R., Gunter, M. E. (2007) Site occupancy in richterite-winchite from Libby, Montana, USA, by FTIR spectroscopy. *Mineralogical Magazine*, **71(1)**, pp. 93-104.
- Ishida, K., Hawthorne, F. C. (2003) Fine structure in the infrared OH-stretching bands of holmquistite and anthophyllite. *Physics and Chemistry of Minerals*, **30**, pp. 330-336.
- Klein, C., Philpotts, A. R. (2013) *Earth Materials – Introduction to Mineralogy and Petrology*. 1<sup>st</sup> ed. Cambridge University Press.
- Kloprogge, J. T., Case, M. H., Frost, R. L. (2001) Raman microscopic study of the Li amphibole holmquistite, from the Martin Marietta Quarry, Bessemer City, NC, USA. *Mineralogical Magazine*, **65(6)**, pp.775-785.
- Kroumova, E., Aroyo, M. I., Perez Mato, J. M., Kirov, A., Capillas, C., Ivantchev, S., Wondratschek, H. (2003) Bilbao Crystallographic Server: useful databases and tools for phase transitions studies. *Phase Transitions*, **76**, Nos. 1-2, pp.155-170.
- Law, A. D., Whittaker, E. J. W. (1981) Studies of the orthoamphiboles. I. The Mössbauer and infrared spectra of holmquistite. *Bulletin de Minéralogie*, **104(4)**, pp. 381-386.
- Leake, B. E., Woolley, A. R., Birch, W. D., Burke, E. A. J., Ferraris, G., Grice, J. D., Hawthorne, F. C., Kisch, H. J., Krivovichev, V. G., Schumacher, J. C., Stephenson, N. C. N., Whittaker, E. J. W. (2003) Nomenclature of amphiboles: additions and revisions to the International Mineralogical Association's 1997 recommendations, *The Canadian Mineralogist*, **41**, pp. 1355-1362.
- Locock, A. J. (2014) An Excel spreadsheet to classify chemical analyses of amphiboles following the IMA 2012 recommendations. *Computers & Geosciences*, **62**, pp. 1-11.
- Markl, G. (2008) *Minerale und Gesteine: Mineralogie – Petrologie – Geochemie*, 2<sup>nd</sup> ed.. Heidelberg: Spektrum Akademischer Verlag.
- Momma, K., Izumi, F. (2008) VESTA: a three-dimensional visualization system for electronic and structural analysis. *Journal of Applied Crystallography*, **41**, pp. 653-658.
- Nasdala, L., Smith, D. C., Kaindl, R., Ziemann, M. (2004) Raman Spectroscopy: Analytical perspectives in mineralogical research. In Beran, A., Libowitzky, E. *Spectroscopic Methods in Mineralogy*. EMU – Notes in Mineralogy, **6**, pp.281-343. Budapest: Eötvös University Press.
- Oberti, R., Hawthorne, F. C., Cannillo, E., Cámara, F. (2007) Long-Range Order in Amphiboles. In Hawthorne, F.C., Oberti, R., Della Ventura, G., Mottana, A. (Eds.), *Amphiboles: Crystal Chemistry, Occurrence, and Health Issues*, **67**, pp. 125-171. Reviews in Mineralogy and Geochemistry, Mineralogical Virginia: Mineralogical Society of America.
- Oberti, R., Cannillo, E., Toscani, G. (2012) How to name amphiboles after the IMA2012 report: rules of thumb and a new PC program for monoclinic amphiboles. *Periodico di Mineralogia*, **81(2)**, pp. 257-267.

- Okrusch, M., Matthes, S. (2014) *Mineralogie*. 9<sup>th</sup> ed.. Springer Spektrum, Berlin Heidelberg.
- Robert, J.-L., Della Ventura, G., Hawthorne, F. C. (1999) Near-infrared study of short-range disorder of OH and F in monoclinic amphiboles. *American Mineralogist*, **84**, pp. 86-91.
- Rull, F. (2012) The Raman effect and the vibrational dynamics of molecules and crystalline solids. In: Dubessy, J., Caumon, M.-C., Rull, F. (Eds.), *Raman Spectroscopy applied to Earth Sciences and Cultural Heritage*. EMU – Notes of Mineralogy, **12**. London: Mineralogical Society of Great Britain & Ireland.
- Schumacher, J. C. (1997) Appendix 2. The estimation of the proportion of ferric iron in the electron-microprobe analysis of amphiboles. *The Canadian Mineralogist*, **35**, pp. 238-246.
- Su, W., Zhang, M., Redfern, S. A. T., Gao, J., Klemd, R. (2009) OH in zoned amphiboles of eclogite from the western Tianshan, NW-China. *International Journal of Earth Sciences*, **98**, pp. 1299-1309.
- Vinx, R. (2008) *Gesteinsbestimmung im Gelände*. 2<sup>nd</sup> ed. Heidelberg: Springer Spektrum.
- Wang, A., Dhameincourt, P., Turrell, G. (1988) Raman and infrared spectroscopic investigation of the cation distributions in amphiboles. *Journal of Molecular Structure*, **175**, pp. 183-188.
- Welch, M. D., Knight, K. S. (1999) A neutron powder diffraction study of cation ordering in high-temperature synthetic amphiboles. *European Journal of Mineralogy*, **11**, pp. 321-331.

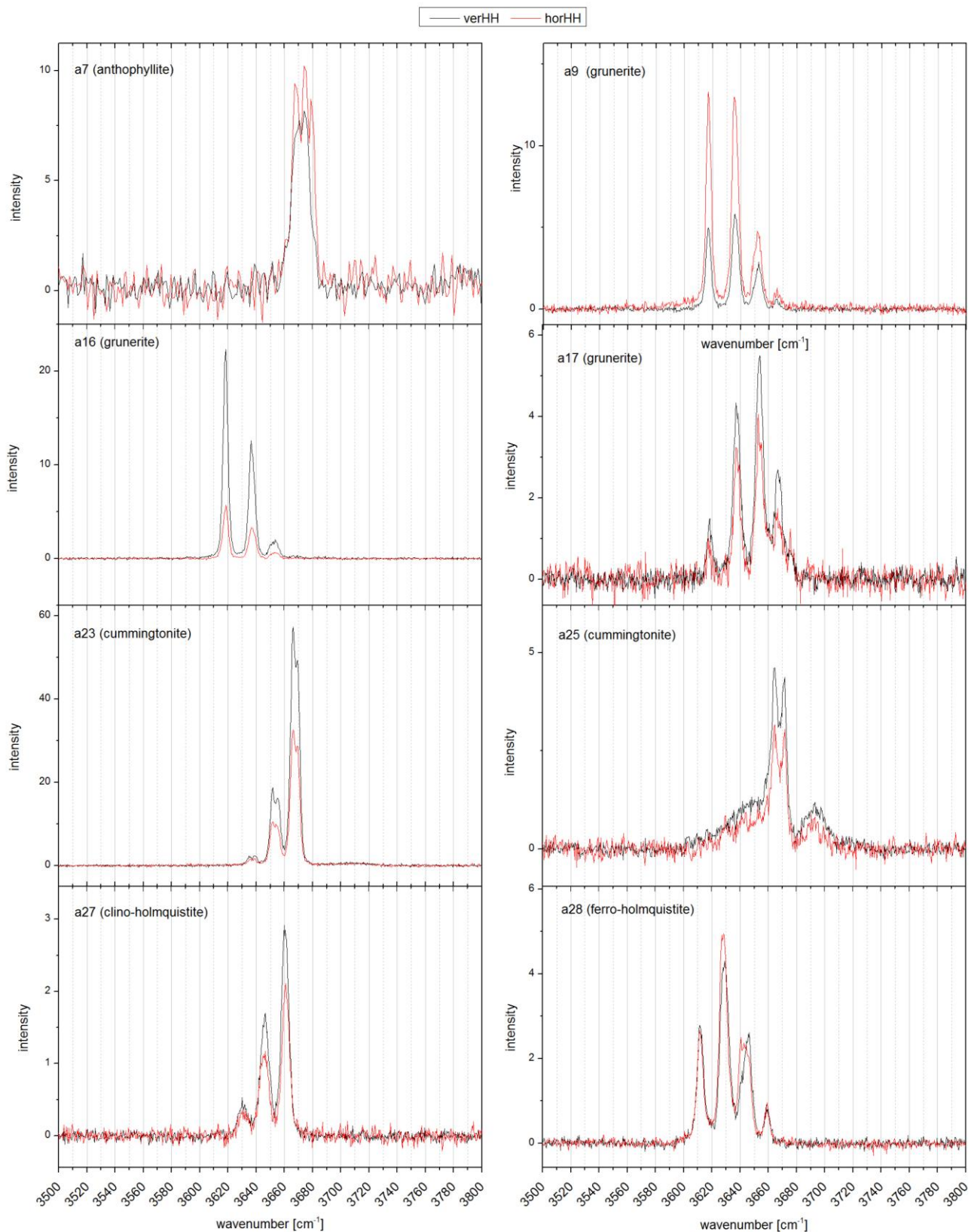
## Internet

- Proram Oberti et al (2012): <http://www.crystal.unipv.it/labcris/AMPH2012.zip>
- Program Locock (2014): <https://github.com/cageo/Locock-2013/releases>
- Mineral data base: [www.mindat.org](http://www.mindat.org)
- Bilbao Server (Kroumova et al., 2003): <http://www.cryst.ehu.es/>

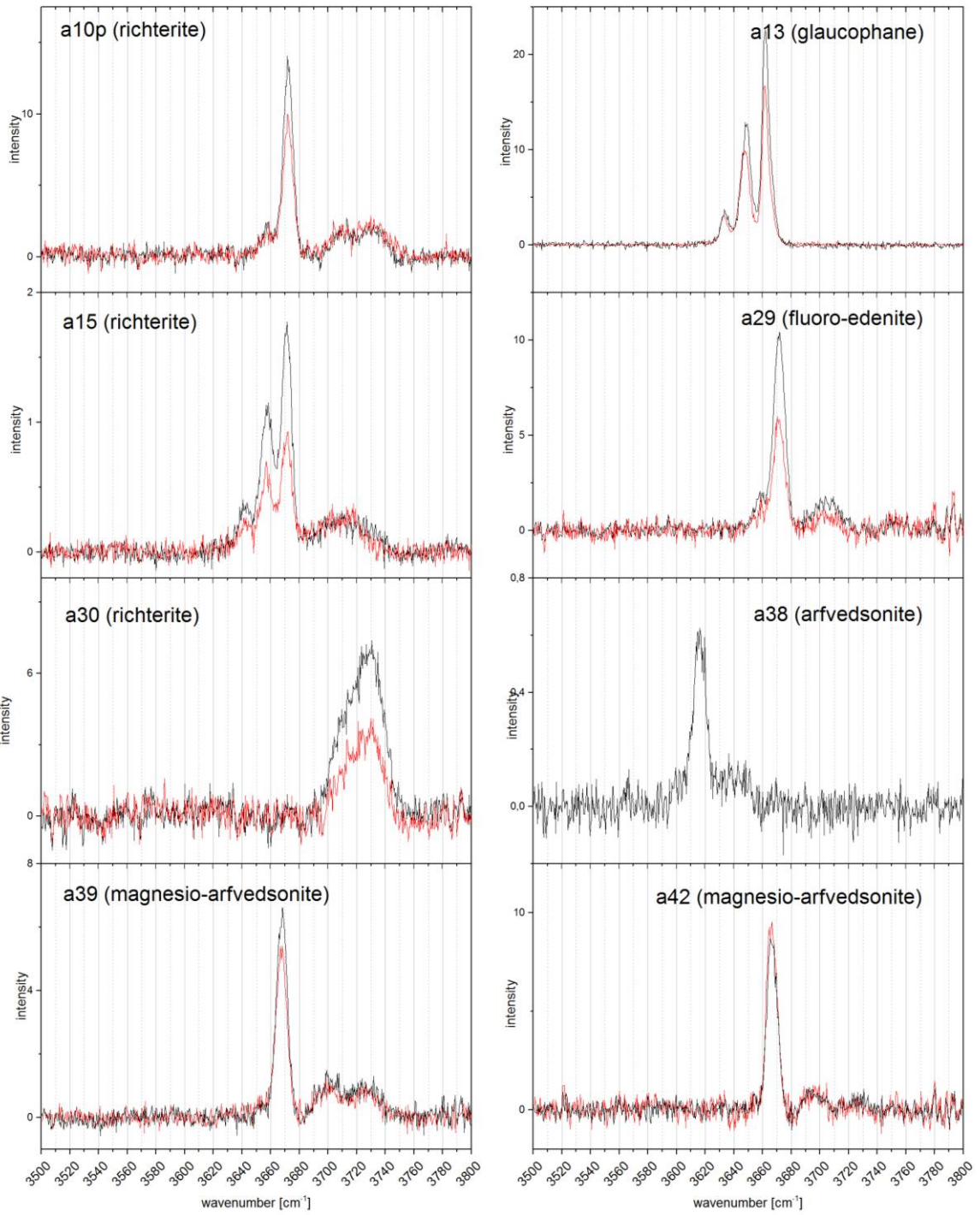
# Appendix



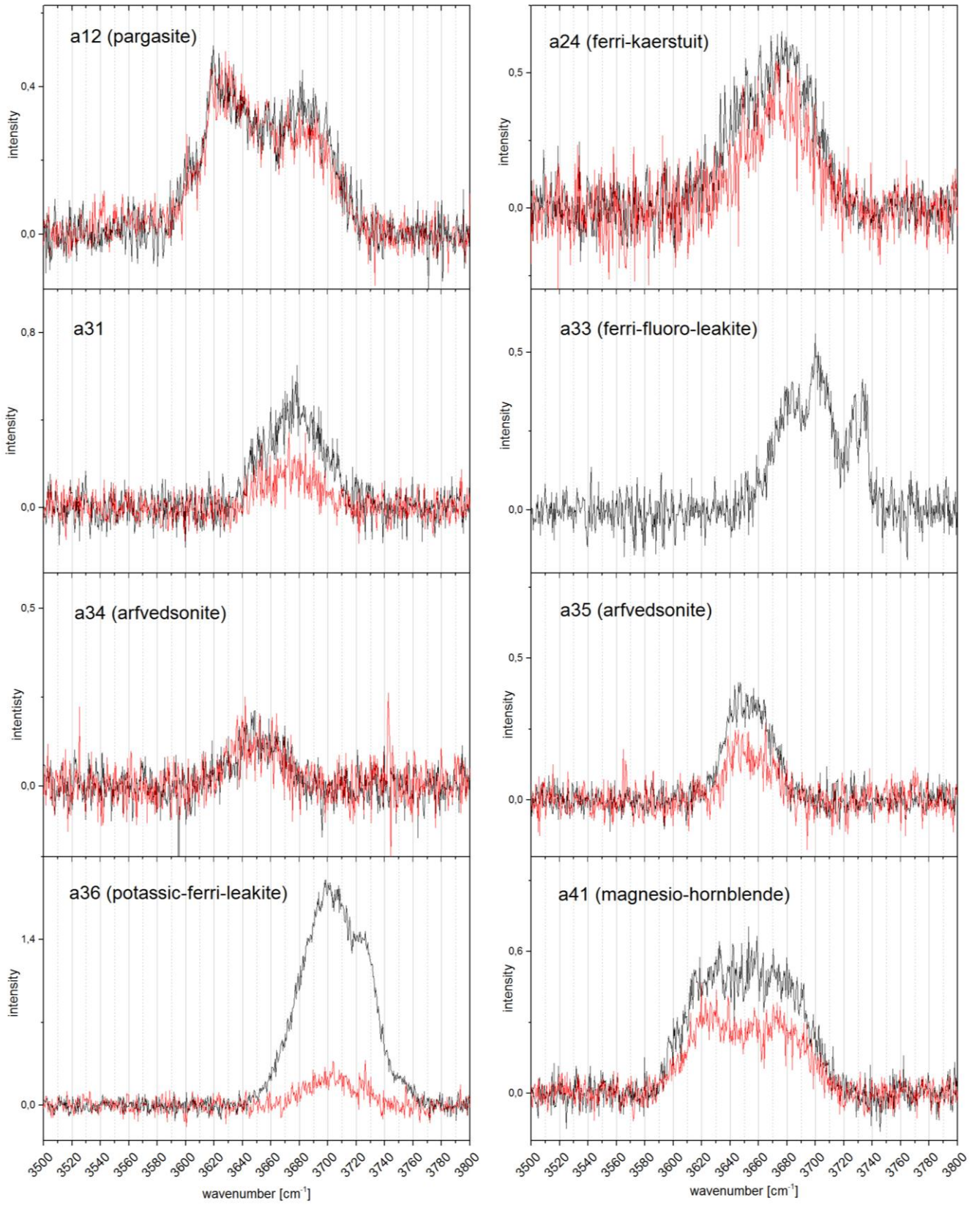




— verHH — horHH



— verHH — horHH



# Erklärung

Hiermit versichere ich an Eides statt, dass ich die vorliegende Arbeit selbstständig verfasst und keine anderen als die angegebenen Hilfsmittel – insbesondere keine im Quellenverzeichnis nicht benannte Internetquellen – benutzt habe. Ich habe die Arbeit bisher nicht in einem anderen Prüfungsverfahren eingereicht. Die eingereichte schriftliche Fassung entspricht der auf dem elektronischen Speichermedium vorliegenden Fassung. Ich bin damit einverstanden, dass ein Exemplar der Abschlussarbeit der Institutsbibliothek zur Verfügung gestellt wird.

Hamburg, den 27.10.2014

# Danksagung

Ich bedanke mich bei Frau PD. Dr. Mihailova, die mir die Anregung zum Thema meiner Masterarbeit gegeben hat. Sie hat mich stets sehr gut betreut, war immer ansprechbereit und hat durch kritische Fragen diese Arbeit positiv weitergebracht. Ein weiterer Dank geht an Herrn Prof. Dr. Schlüter für die gute Betreuung sowie die Beratung bei allen mineralogischen Fragestellungen.

Nicht zuletzt sei gedankt Frau Steffi Heidrich und Herrn Peter Stutz für die Mikrosonden-Messungen sowie die Präparation der Proben. Des Weiteren möchte ich Frau Dr. Anke Watenpuhl danken, für ihre hilfreichen Diskussionen sowie die Korrekturen von Präsentation und Poster, die im Rahmen dieser Masterarbeit entstanden sind und die Hilfe bei allen Fragen der akademischen Welt.

Außerdem will ich mich bedanken bei meinen Freunden Larissa, Paula, Kurt, Zuzana, meiner Schwester Lena und meinen Kommilitonen André, Karol und Siegfried für Diskussionen, einem gesunden Maß an Ablenkung und das gemeinsame Studium. „Last but not least“ will ich meinen Eltern für ihren Rückhalt und ihre stetige Unterstützung danken.